Spreading and rebound dynamics of sub-millimetre urea-water-solution droplets impinging on substrates of varying wettability

Martin Wörner[1,*] Nima Samkhaniani[2], Xuan Cai[2,3], Yanchen Wu[3,#], Arijit Majumdar[1],

Holger Marschall[4], Bettina Frohnapfel[2], Olaf Deutschmann[1,3]

[1] Karlsruhe Institute of Technology (KIT), Institute of Catalysis Research and Technology,

Engesserstr. 20, 76131 Karlsruhe, Germany

[2] Karlsruhe Institute of Technology (KIT), Institute of Fluid Mechanics,

Kaiserstr. 10, 76131 Karlsruhe, Germany

[3] Karlsruhe Institute of Technology (KIT), Institute for Chemical Technology and Polymer Chemistry,

Engesserstr. 20, 76131 Karlsruhe, Germany

[4] Technical University Darmstadt, Computational Multiphase Flows,

Alarich-Weiss-Straße 10, 64287 Darmstadt, Germany

Present address: Karlsruhe Institute of Technology (KIT), Institute of Applied Materials Science,

Straße am Forum 7, 76131 Karlsruhe, Germany

* Corresponding author: Martin Wörner, E-mail: martin.woerner@kit.edu,

Phone +49 721 608 47426, Fax: +49 721 608 44805

Abstract

The interaction of droplets consisting of urea-water solution (UWS) with a wall is of interest for automotive exhaust gas after-treatment of Diesel engines by selective catalytic reduction (SCR). Since the impingement of tiny UWS droplets on the solid substrate is difficult to examine experimentally, little is known about the detailed dynamics of this process. In the present study, the normal impact of single UWS droplets impinging on dry solid substrates of greatly differing wettability is investigated numerically under axisymmetric conditions. Simulations are performed by a diffuse interface phase-field solver developed by the authors where the coupled Cahn-Hilliard Navier-Stokes equations are solved using OpenFOAM. The code is thoroughly validated against a number of experiments from literature considering the rebound of millimetre-sized water droplets from hydrophobic substrates.

The numerical simulations on the impact dynamics of UWS droplets cover wide ranges of sub-millimetre droplet sizes and impact velocities that are relevant in technical SCR systems. A strong influence of substrate wettability on droplet dynamics is identified. Reducing wettability from hydrophilic to superhydrophobic conditions reduces spreading and enables drop rebound with reduced drop-surface contact time. The effects of drop diameter, drop impact velocity and equilibrium contact angle on the maximum spreading ratio are quantified, and regime maps on rebound versus non-rebound (deposition) impact outcomes are provided. The results of the present interface-resolving numerical simulations may be useful for development of more advanced drop-wall interaction models as they are required in CFD codes relying on the Euler-Lagrange approach for large-scale computations of UWS sprays.

1   Introduction

The emission of nitrogen oxides (NO_x) from Diesel engines is a major problem in air pollution, affecting environment and society. One of the most favorable technologies to reduce NO_x is Selective Catalytic Reduction (SCR) [1, 2]. In this process, ammonia serves as reducing agent to convert pollutant NO_x into harmless nitrogen and water [3]. In passenger cars, ammonia is not supplied directly in gaseous form for security issues. Instead, a spray of urea-water-solution (UWS) is injected into the hot exhaust upstream of the SCR catalyst. Ammonia is then provided through evaporation and thermal decomposition of urea (CH_4N_2O). A static mixer device mounted downstream of the injector serves for secondary atomization and enhances heat transfer to the droplets. Due to compact design requirements, spray impingement on the exhaust pipe wall downstream the mixer is unavoidable [4, 5]. Impacting droplets locally cool the wall and may form a liquid film [6]. As water evaporates from the solution, urea reaches a critical concentration that promotes crystallization [7]. As a result, there is an enhanced risk for undesired intermediates and by-products forming solid deposits [8, 9]. Therewith, the system efficiency deteriorates in terms of decreased NO_x conversion and increased pressure drop.

Computational fluid dynamics constitutes a valuable tool to support the optimization of automotive SCR-systems at various operating conditions [10-14]. The spray is typically modelled with a statistical Lagrange approach in combination with an Eulerian approach for the gas phase, being based either on the Reynolds-averaged Navier-Stokes equations or on large eddy simulation. Due to the complex physics of the drop impingement process, such simulations rely upon empirical models known as impingement maps [15]. Impingement outcomes are generally classified as *deposition* (the droplet spreads and recoils while adhering to the wall), *splash* (the droplet is disintegrated into smaller ones) and *rebound* (the droplet bounces from the wall). Splash might be further divided into prompt and corona type splash while rebound can be classified into partial and complete rebound [16]. The borders of the different regimes depend on hydrodynamic parameters and temperature and their knowledge are important ingredients for modeling of spray wall interaction in CFD simulation for SCR applications. From the various impingement outcomes, all but complete rebound contribute to liquid film formation.

There is still an uncertainty regarding impingement modelling for SCR applications, particularly in the range of the Leidenfrost temperature that separates wall wetting and non-wall wetting regimes due to thermally induced rebound [17]. Therefore, improvement of multi-regime impingement models for SCR applications is an actual topic of research [18-20]. Clearly, a deeper understanding of the drop-wall interaction is a basic requirement to calibrate CFD models in order to improve their prediction accuracy for automotive SCR applications. Typical diameters of UWS droplets in SCR applications are of order 100 µm. The detailed dynamics of such tiny UWS droplets as they impinging on the solid substrate is difficult to examine experimentally due to the required high spatial resolution.

Physically, the drop wall-interaction is strongly influenced by surface characteristics such as wettability and roughness. On an ideal surface, a static sessile droplet exhibits a unique equilibrium contact angle (θ_e). For non-ideal real surfaces showing surface inhomogeneity, the droplet has no unique contact angle but exhibits a range of contact angles on the surface depending on roughness. The difference between the advancing (maximum) contact angle (θ_a) and the receding (minimum) contact angle (θ_r), both observed on a scale much larger than the scale of the surface inhomogeneity/roughness, is commonly denoted as contact angle hysteresis ($H_\theta = \theta_a - \theta_r$). Modeling approaches differ in how the contact angle is implemented as the boundary condition at the contact line and how this contact angle empirically depends on the contact line speed [21]. Today, there is no consensus on how to model the dynamic contact angle on a fundamental level.

The goal of the present paper is to identify favorable physical parameters for achieving hydrodynamic rebound of UWS droplets in the SCR exhaust gas pipe by interface-resolving numerical simulation. Drop rebound significantly reduces contact time between drop and wall, thereby minimizing local wall cooling and reducing the risk for film and deposit formation. A well-known measure to induce drop rebound is the use of hydrophobic surfaces. As droplet impact on dry solid surfaces is important in various applications, it has been studied intensively as summarized in recent reviews [22, 23]. Depending on wall wettability (θ_e, H_θ), physical properties of the liquid (density ρ_L, dynamic viscosity μ_L, and surface tension σ), drop diameter (D_0) and drop impact velocity (U_0), different impingement outcomes can be observed.

Due to its importance for technical applications such as self-cleaning or anti-icing [24], the development of hydrophobic ($90° < \theta_e < 150°$) or superhydrophobic ($\theta_e > 150°$, $H_\theta < 10°$) surfaces with drop rebound after impingement has attracted significant attention in the last few decades. Superhydrophobic surfaces can be designed by enhancing hydrophobic surfaces by addition of roughness or a certain kind of morphology [25]. When a droplet impinges a superhydrophobic surface with low wetting hysteresis, it deforms under small energy dissipation storing kinetic energy, which will make the droplet recoil. Mao et al. [26] were among the first who investigated droplet rebound experimentally and concluded that low viscosity, high impact velocity and large contact angle increase the tendency for rebound. Later on, detailed experimental visualizations of dynamic droplet impact and rebound process were reported by several research groups [27-32]. Antonini et al. [33] highlighted in an experimental study the important role of the receding contact angle (θ_r) for obtaining drop rebound which occurs only for $\theta_r > 100°$.

As a powerful complement to experimental approaches, interface-resolving (direct) numerical simulations can be used to investigate droplet impact. Although most numerical studies consider droplet deposition or splash on hydrophilic surfaces, a few studies on droplet rebound dynamics exist. Various numerical methods for interface representation are used to simulate the droplet impact process and explore ranges of physical parameters leading to rebound. These include the volume-of-fluid [21], moment-of-fluid [34], level-set [32, 35], phase-field [36, 37], Lattice-Boltzmann [38] and Lagrangian-Eulerian moving mesh [39, 40] approaches. In numerical studies with the latter methods, often millimetre-size droplets with moderate impact velocity are considered whereas molecular dynamics simulations are restricted to nano-scale droplets [41]. Spray atomization, however, creates UWS droplets with diameter in the range $20-180$ μm [42] and mean wall-normal velocities of the droplets up to 20 m s^{-1} [43]. Similar conditions are encountered in drop-on-demand inkjet printing, where few experimental studies on impact dynamics exist for hydrophilic surfaces [44]. Numerically, the behaviour of such tiny droplets is seldom investigated and studies are limited to a few representative cases [36, 39, 45, 46].

Thus, the focus of the present numerical study is on the impact of UWS droplets in the range of practically relevant sizes and velocities. For numerical simulation, we employ a phase-field method that solves the coupled Cahn-Hilliard Navier-Stokes equations by a finite volume discretization implemented in OpenFOAM [47]. The underlying code *phaseFieldFoam* developed by the authors exhibits very low parasitic currents [48] (which is essential for simulations of sub-millimetre droplet sizes) and was validated for various wetting phenomena [47, 49]. In particular, we have carried out three-dimensional (3D) simulations of droplet rebound from a structured hydrophobic substrate where the micro-grooves are geometrically resolved [50]. Furthermore, the code has been used to study conditions where bubble formation during liquid back suction of UWS from the delivery line into the UWS storage tank is avoided [51]. Last but not least, the code has been validated for the impact of millimetre-size UWS droplets on a hydrophilic surface resulting in deposition [52].

To cover a wide parameter range at reasonable computational costs, the following assumptions are made: (i) the orthogonal impact of a single droplet on an ideally smooth dry horizontal surface is considered, (ii) the conditions are non-evaporative and isothermal with constant physical properties corresponding to atmospheric temperature and pressure, and (iii) the entire impingement process is axisymmetric. Under these simplifications, the effects of droplet diameter ($25-800$ μm), impact velocity ($0.01 - 10$ m s^{-1}) and surface wettability (equilibrium contact angle $30-170°$) are investigated by a large number of simulations. Impact maps separating deposition and rebound regimes are generated in terms of the above parameters. These regime maps can be useful for design and optimization of UWS spray impingement so that solid deposit formation is reduced by maximizing UWS droplet rebound.

The remainder of this paper is organized as follows. Section 2 introduces the numerical methodology including the governing equations the computational setup. Section 3 presents a thorough validation for the impact and rebound of water droplets. In Section 4 impact and rebound of UWS droplets are investigated for a wide parameter range. Section 5 is devoted to summary and conclusions.

2   Numerical methodology

2.1   Governing equations

The phase-field method is particularly suitable for the present study given its capability of properly modelling contact line motion [47, 53-55], a central problem involved in the droplet impact and rebound process. In this method, an order parameter (C) is used to describe the distribution of the liquid (L) and gas (G) phases. For the bulk phases, the order parameter is set to distinct values as $C_\mathrm{L} = 1$ and $C_\mathrm{G} = -1$ while it varies rapidly but smoothly in a thin transition layer (the diffuse interface). The spatial and temporal evolution of the order parameter is governed by the convective Cahn-Hilliard equation

$$\partial_t C + (\mathbf{u} \cdot \nabla)C = M \nabla^2 \phi. \tag{1}$$

Here, subscript t denotes time derivative, $\mathbf{u}$ the velocity field, M the Cahn-Hilliard mobility and ϕ the chemical potential

$$\phi = \frac{\lambda}{\varepsilon^2} C(C^2 - 1) - \lambda \nabla^2 C. \tag{2}$$

In. Eq. (2), ε is the capillary width that determines the thickness of the diffuse interface and λ is the mixing energy density. For an equilibrium system and a planar interface, λ can be related to ε and surface tension σ as [54]

$$\lambda = \frac{3\sqrt{2}\sigma\varepsilon}{4} \tag{3}$$

Since the surface tension σ can be known from experiment measurements and λ can be determined through Eq. (3), an appropriate value for ε needs to be chosen only. It is commonly determined in relation to a characteristic macroscopic length scale of the flow problem, here the initial drop diameter. The ratio of both length scales constitutes the Cahn number $Cn = \varepsilon/D_0$.

To ensure that the diffusive flux on the right hand side of the Cahn-Hilliard Eq. (1) is approaching to zero as ε is approaching zero, i.e. in the sharp interface limit $\varepsilon \to 0$, the mobility is specified as

$$M = \chi \varepsilon^2. \tag{4}$$

There, χ is a constant pre-factor [56]. In practice, χ can be chosen by fitting experimental data [49, 57].

At the solid wall, the diffusive flux in Eq. (1) allows for motion of the contact line in combination with a no-slip boundary condition (used here) without giving rise to the singularity of the shear stress [53, 58]. Using the wall free energy formulation at local equilibrium, one obtains the following Neumann boundary condition for the order parameter that accounts for the solid surface wettability by the equilibrium contact angle θ_e [59]

$$\mathbf{n}_s \cdot \nabla C = \frac{\sqrt{2}}{2} \frac{\cos \theta_e}{\varepsilon} (1 - C^2). \tag{5}$$

Here, $\mathbf{n}_s$ is the outward unit normal to the solid surface. In the Appendix it is shown, that although the equilibrium contact angle is specified as a boundary condition, the actual contact angle of the moving contact line may differ from the equilibrium contact angle during the spreading process. This observation is in agreement with numerical studies from literature. In references [54, 60] it is found that this energy equilibrium boundary condition can recover the hydrodynamic wetting theory of Cox [61], which is regarded as a representative dynamic contact angle model [62, 63]. Approaches that explicitly model non-equilibrium at the contact line by a time-dependent (relaxation) boundary condition at the solid surface [53, 64, 65], as used e.g. in the computations in [66], are not considered here.

In the present study, the gas and liquid phases are considered as immiscible, incompressible, isothermal Newtonian fluids. Therefore, the flow can be described by the continuity equation and single-field Navier-Stokes equation

$$\nabla \cdot \mathbf{u} = 0, \tag{6}$$

$$\partial_t (\rho_C \mathbf{u}) + \nabla (\rho_C \mathbf{u}\mathbf{u}) = -\nabla p + \nabla \cdot \left[\mu_C \left(\nabla \mathbf{u} + (\nabla \mathbf{u})^T \right) \right] + \mathbf{f}_\sigma + \rho_C \mathbf{g}. \tag{7}$$

Here, p is the pressure and $\mathbf{g}$ the gravity vector. The interface energy term $\mathbf{f}_\sigma$ is considered with the formulation

$$\mathbf{f}_\sigma = \phi \nabla C. \tag{8}$$

The density and viscosity are computed based on the order parameter using an arithmetic mean

$$\rho_C = \frac{1+C}{2} \rho_L + \frac{1-C}{2} \rho_G, \quad \mu_C = \frac{1+C}{2} \mu_L + \frac{1-C}{2} \mu_G. \tag{9}$$

Here, ρ_G and μ_G denote the density and viscosity of the gas phase, respectively. Through Eqs. (8) and (9), the Navier-Stokes Eq. (7) and the Cahn-Hilliard Eq. (1) are coupled.

The above system of equations was implemented as a top-level solver *phaseFieldFoam* in the platform *foam-extend*, a community-driven version of the open-source CFD software OpenFOAM®. It is solved by a segregated algorithm as described in [51]. For details on numerical implementation and validation of *phaseFieldFoam*, the reader is referred to [47-52] and a forthcoming publication by Marschall et al. [67].

2.2 Computational setup

Figure 1 shows a sketch of the computational set-up. All the simulations in the present study are carried out assuming axial symmetry. The computational domain is a 3D wedge (angle 4°) of radial width W and height H. We have checked for representative cases that results are unaffected by the chosen domain size. The drop prior to impact is assumed spherical with diameter D_0 having a spatially uniform downward velocity U_0. The droplet centroid is located at $D_0/2$ above the solid surface so that the droplet has point contact with the surface. At the bottom solid surface, the boundary conditions are set as no-slip for the velocity field in combination with Eq. (5) for the order parameter. At the right boundary (side wall) a no-slip condition applies for the velocity field in combination with a zero normal gradient condition for the order parameter (corresponding to a neutral contact angle of 90°, although this wall is never wetted in the course of the simulations). At the top boundary (atmosphere in Figure 1), a zero normal gradient condition for the order parameter and zero relative pressure are combined with an inlet/outlet boundary condition for velocity (flow out of the domain assigns a zero normal gradient condition, while flow into the domain assigns a velocity based on the flux normal to the boundary).
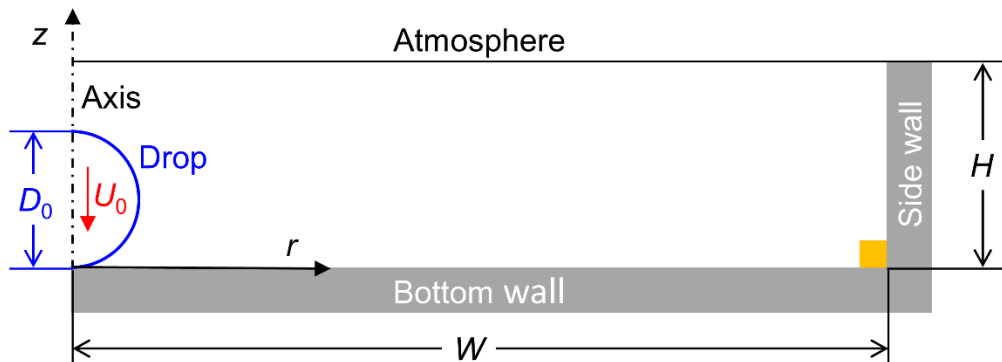
Figure 1: Sketch of computational setup with initial drop position. The orange square in the lower right corner serves to illustrate mesh resolution. In this study, most simulations are performed with a resolution of the orange square by 10×10 uniform grid cells (corresponding to $Cn = 0.02$ and $N_{di} = 8$, see below).

Phase-field methods require adequate resolution of the diffusive interface. For a planar interface at static equilibrium, the solution of Eq. (1) follows a hyperbolic tangent profile where the variation of C between ± 0.9 occurs over a distance of about 4ε. Here, we discretize the computational domain by a uniform grid with equal mesh size h in radial (r) and vertical (z) direction. The diffuse interface is thus resolved by $N_{di} = 4\varepsilon/h$ mesh cells. Experience from previous studies indicates that simulation results become insensitive on ε and h when the conditions $Cn \leq 0.02$ and $N_{di} \geq 6$ are met simultaneously. Here, the effects of Cahn number Cn and diffuse interface resolution N_{di} are investigated in Section 3.1.1 and quantified by comparison with experimental data. In all present simulations, the mobility pre-factor is set to $\chi = 1$ m s kg^{-1}. In a previous study [50] it was shown that reducing χ to 0.4 m s kg^{-1} has only a slight effect on spreading dynamics and maximum spreading.

For the present computations, the following numerical schemes are used. A high-resolution scheme (Gauss Gamma [68]) is employed for spatial derivatives. For time integration, a second-order two-time-level backward scheme is generally used while for high impact velocities a first order Euler bounded schemes has proved to be favourable. The time step Δt is adaptive during the simulation and limited by an upper bound of the Courant number $Co = u_{max}\Delta t/h \leq 0.05$, where u_{max} denotes the magnitude of the maximum velocity in the computational domain. The physical properties of both phases vary slightly from case to case as given in Sections 3 and 4.

10

The numerical results are physically interpreted in terms of the relevant non-dimensional groups. These are the impact Weber number ($We = \rho_L D_0 U_0^2 / \sigma$) describing the ratio between inertial and capillary forces and the impact Reynolds number ($Re = \rho_L D_0 U_0 / \mu_L$) constituting the ratio between inertial and viscous forces. A further (dependent) non-dimensional number is the Ohnesorge number $Oh = \mu_L / \sqrt{\rho_L \sigma D_0} = \sqrt{We}/Re$. The Ohnesorge number is especially useful in combination with We. As Oh does not involve a velocity scale, it is a constant for a drop of given diameter.

3   Validation for rebound of water droplets

The purpose of this section is to validate the numerical method and code for the normal impact of a single droplet on a hydrophobic surface. Possible outcomes of the impingement process are complete rebound, partial rebound and deposition. Experiments with rebound of sub-millimetre size single droplets are not available in literature to the best of our knowledge. Therefore, three experiments from literature for droplets of mm size are used for validation. All experiments show complete rebound but differ with respect to gas entrapment. The experiment of Shen et al. [69] is used to study the influence of numerical parameters. Having the numerical parameters fixed, experiments from Lin et al. [70] showing bubble entrapment are recalculated. Often, droplet rebound is characterized by the contact (or rebound) time T_{ct}, which is measured between the drop/surface first contact and take off from the substrate. As further validation, simulations for sub-millimetre droplets are performed to compare the contact time of the droplet with correlations of Richard et al. [71] obtained for larger droplets.

3.1   Temporal evolution of droplet morphology and spreading ratio

During spreading, the drop morphology changes. This is illustrated by comparing drop shapes at different instants in time. Furthermore, the process is quantified by the time evolution of the spreading ratio $\beta = \beta(t) = D_{wet}(t)/D_0$, where $D_{wet}(t)$ is the instantaneous diameter of the wetted circular area (contact diameter). Of special interest for technical applications are the maximum spread ratio $\beta_{max} = \beta(t_{max})$ at the end of the advancing spreading phase and the corresponding time t_{max} since both are important for estimating the heat transfer with the solid surface (a subject of future study).

11

3.1.1 Experiment of Shen et al. (2018)

Shen et al. [69] studied the impact of deionized water droplets ($D_0 = 2$ mm) on a superhydrophobic surface ($\theta_e = 161°$) focusing on the influence of temperature and impact velocity. Here, an experiment at room temperature with impact velocity $U_0 = 0.5$ m s^{-1} is chosen for validation. The simulations are performed with $\rho_L = 996$ kg m^{-3}, $\mu_L = 1$ mPa s, $\sigma = 71$ mN m^{-1} resulting in $We = 7$. The dimensions of the computational domain are $W/D_0 = 1.5$ and $H/D_0 = 3$. Keeping $\chi = 1$ m s kg^{-1} fixed, we study the influence of Cahn number ($Cn = 0.01$ and 0.02) and grid resolution ($N_{di} = 8$ and 16). Note that with fixed value of χ, the variation of Cn results in a variation of mobility as well, namely $M = 4 \times 10^{-10}$ m^3 s kg^{-1} and $M = 16 \times 10^{-10}$ m^3 s kg^{-1}, respectively. For further reference, this test case is denoted as Case A.

The numerical and experimental results are compared in Figure 2. Figure 2 a) shows experimental and computed drop shapes ($Cn = 0.02$, $N_{di} = 8$) for different instants in time. For $t = 2$ ms and $t = 3.6$ ms, the droplet shapes are very similar. While $t = 2$ ms corresponds to the advancing phase of spreading and $t = 3.6$ ms to the receding phase, the experimental spreading ratio for both instants in time is almost identical, see dashed red lines in Figure 2 (a). For the later instants in time, $t = 7.2$ ms and $t = 11$ ms, some differences of droplet shape in experiment and simulation can be observed.

The comparison of the spreading ratio in Figure 2 (b) includes numerical results for three cases. In order to calculate the spreading ratio, a radial sampling line at a vertical position $z = D_0/100$ above the surface is considered. The instantaneous wetting diameter $D_{wet}(t)$ is calculated from the maximum radial position along the sampling line where the order parameter is zero. Up to $t \approx 8$ ms, simulations with different parameters yield very similar results and the spread factor β is in good agreement with experimental data. For larger times, deviations from the experimental contact time of about 10.4 ms are observed depending on Cahn number. For a fixed Cahn number $Cn = 0.02$, doubling interface resolution (by reducing h by a factor of 2) has only a very small effect on the time evolution of the spread ratio yielding a contact time of about 9 ms. Reducing the Cahn number to $Cn = 0.01$ while keeping the interface resolution $N_{di} = 8$ fixed reduces contact time to about 8 ms.

The reason for this difference in contact time can be understood by a detailed comparison of the time evolution of the droplet shapes provided in the Supplemental Material A. It turns out that the reduced contact time in the simulation with $Cn = 0.01$ is related to a temporary dewetting (dryout) of the impact centre, which is not observed for $Cn = 0.02$. As consequence, the droplet in the simulations with $Cn = 0.01$ temporarily adopts a ring shape (torus) with subsequent formations of one bubble being attached to the surface and one bubble floating in the bouncing drop, cf. Figure 3 (a) and Subsection 3.1.2. No such bubble entrapment is observed in the experiment [69] or in the simulations with $Cn = 0.02$. While the overall behaviour of the drop impact and rebound process in simulations with $Cn = 0.01$ and $Cn = 0.02$ is very similar, some details such as rupture of the central liquid film resulting in dewetting are captured only for $Cn = 0.01$, where the thickness of the diffuse interface is reduced.

A criterion for dryout of the central liquid film formed during drop impact on flat hydrophobic surfaces derived from numerical simulations is given by Renardy et al. [72]. Accordingly, dewetting occurs provided the Weber number exceeds a critical value given by

$$We_{\text{dry}} = 2\left[\frac{1590}{(0.5Re)^{1.49}} + 3.62\right]. \tag{10}$$

For the present case ($We = 7$, $Re = 996$), Eq. (10) yields $We_{\text{dry}} = 7.5$ indicating no dryout. As the difference between both Weber numbers is small, the conditions of Case A may correspond to the transition range between dryout and no dryout. Interesting with respect to dryout are also findings of a recent experiment by Chantelot et al. [73]. There, dewetting of the impact center is enforced by a dedicated point-like superhydrophobic spherical macro-defect. Puncture of the liquid film occurs when the size of the defect is close to the film thickness. The collision between opposing rims creates upward momentum leading to torus like bouncing and reduced contact time, similar as observed in the present simulations.
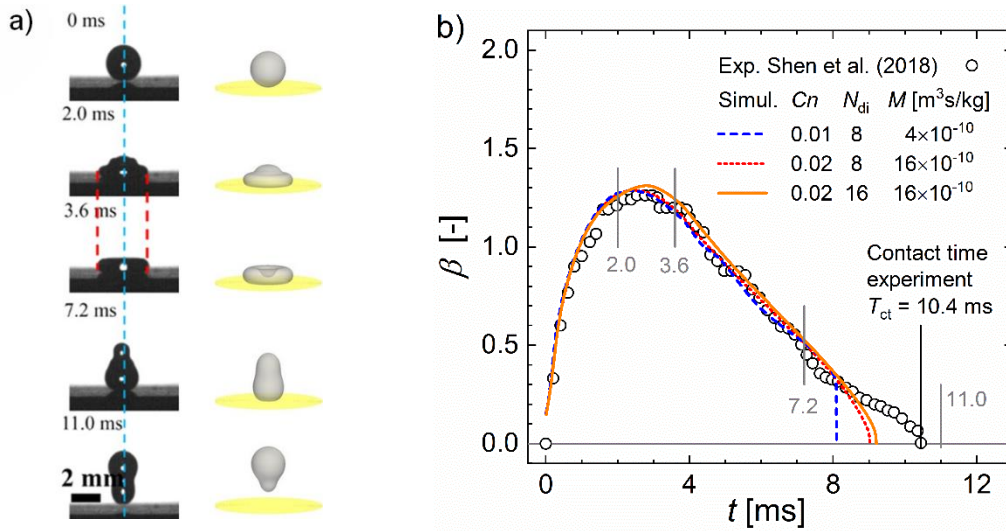
Figure 2: Comparison of numerical results with experiment from Shen et al. [69] ($\theta_e = 161°$, $D_0 = 2$ mm, $We = 7$, $Re = 996$). (a) Droplet shape at different instants in time (left: exp., right: simulation with $Cn = 0.02$, $N_{di} = 8$), (b) time evolution of spreading ratio. The sudden decrease of β at 8 ms in the simulation with $Cn = 0.01$ is related to a temporary dewetting of the impact center which is not observed in the simulations with $Cn = 0.02$ where the diffuse interface is thicker.

3.1.2   Experiment of Lin et al. (2018)

Chen et al. [74] experimentally investigated the effects of surface wettability on bubble entrapment during droplet impingement on solid surfaces for relatively low impact velocities. Figure 3 (a) shows the obtained regime map as function of Weber number and surface wettability. The authors report that bubble entrapment occurs only on sufficiently hydrophobic surfaces within a narrow range of impact velocities. For drop impact on hydrophobic surfaces, the entrapped bubble stays attached to the surface (red bullets). For drop impact on superhydrophobic surfaces resulting in rebound, the bubble is trapped in the top of the bouncing droplet (blue bullets). For symbols other than "blue bullet", i.e., red bullet and star, the impact outcome is not apparent from Figure 3 (a). Depending on conditions, it may be a full or partial rebound or deposition.

In this subsection, we reproduce the different bubble entrapment behavior numerically and validate the results against experiments of Lin et al. [70], who report a series of experimental studies on impact dynamics of glycerol-water mixture droplets on surfaces of different wettability. Here, the

14

impingement of a pure water droplet ($D_0 = 2$ mm) is considered for three distinct cases. For Cases B
and C, the contact angle is $161°$ with impact velocities of 0.3 and 0.65 m s^{-1}, respectively. For case D,
it is $\theta_e = 106°$ and $U_0 = 0.52$ m s^{-1}. The simulations are performed with $\rho_L = 997$ kg m^{-3}, $\mu_L =$
0.9 mPa s, $\sigma = 71.8$ mN m^{-1} yielding Weber numbers 2.5, 11.7 and 7.5 for cases B, C and D,
respectively. The dimensions of the computational domain are $W/D_0 = 1.5$ and $H/D_0 = 3$. The
numerical parameters are $Cn = 0.02$ and $\chi = 1$ m s kg^{-1} with interface resolution $N_{di} = 8$. Table 1
gives a concise comparison of the parameters in the different cases.

Table 1: Comparison of conditions for Cases A-D. Parameters which are identical for all cases
are $D_0 = 2$ mm, $\rho_G = 1$ kg m^{-3}, $\mu_G = 1.48 \times 10^{-5}$ Pa s, $\chi = 1$ m s kg^{-1}, $W/D_0 = 1.5$, $H/D_0 = 3$.

Case	U_0	We	Re	θ_e	Cn	M	N_{di}
	m s^{-1}	-	-	°	-	m^3 s kg^{-1}	-
A	0.50	7.0	996	161	0.01	4×10^{-10}	8
	0.50	7.0	996	161	0.02	16×10^{-10}	8
	0.50	7.0	996	161	0.02	16×10^{-10}	16
B	0.30	2.5	665	161	0.02	16×10^{-10}	8
C	0.65	11.7	1440	161	0.02	16×10^{-10}	8
D	0.52	7.5	1152	106	0.02	16×10^{-10}	8

Figure 3 (b) displays the time evolution of the droplet shape for Case B. Overall, the deformation
and rebound is very similar to that of case A. Owing to the smaller Weber number of Case B, the
dimple in the impact center at time of maximum spreading is less pronounced as compared to Case A,
cf. Figure 2 (a) for $t = 3.6$ ms. In Figure 3 (c) and (d), the time evolution of droplet shapes in
experiment [70] and simulation are compared for cases C and D, respectively. For case C, capillary
waves travel to the top of the drop [75] yielding a pyramidal structure [72, 76] with several stair-like

steps ($t = 1.44$ ms). As the drop spreads on the surface, these steps merge and form a pancake structure with a dimpled air cavity inside ($t = 3.44$ ms). Close to maximum spreading, the air cavity in the center of the drop is close to cylindrical with dewetting of the surface ($t = 3.84$ ms). During the receding stage, the liquid is rushing back, the interface in the cavity adhering to the surface ($t = 4.24$ ms). As the upper part of the cavity collapses, a bubble is entrapped accompanied by ejection of a thin liquid jet ($t = 4.64$ ms). The entrapped bubble rises within the drop ($t = 9.44$ ms) which then rebounds from the surface ($t = 13.5$ ms). While the capillary width (ε) is too large to reproduce the thin jet, all other main phenomena during the drop impact on the surface are captured reasonably well in the simulation. Some difference between numerical and experimental results on the bubble size can be attributed to the optical effect from the light refraction by the curved interface of the droplet in the experimental study [70].

A behavior very similar to Figure 3 (c) and (d) was already described almost 50 years ago by Elliott & Ford [77]. These authors performed experiments of drop impact on smooth paraffin wax surfaces ($\theta_e = 103°$) and divided the process in eight stages. For Stage III (Involution) it is noted: "The central tip involuted and drained a central area within the drop and, as retraction forces operated, the liquid closed over the drained area trapping a small air bubble within the drop". This is exactly what is observed for Case C in the period $t = 3.44–4.64$ ms and for Case D in the period $t = 5.25–6.2$ ms. For case D, the entrapped bubble sticks to the solid surface ($t = 7.25$ ms) similar to the sketches in Fig. 2 in [77]. For Stage IV (Retraction) Elliott & Ford [77] note: "With larger drops and/or heights of fall the air bubble was broken up and a portion rose to the drop surface". This is similar to what is observed here for Case C at $t = 9.44$ ms, and in the simulation for Case A with $Cn = 0.01$. While Elliott & Ford [77] did not observe drop rebound for the contact angle $\theta_e = 103°$ used in their experiments, the superhydrophobic surface of Case C ($\theta_e = 161°$) results in rebound so that for $t = 9.44$ ms the floating bubble within the bouncing drop is observed.

As mentioned before in the discussion of Case A, dryout of the central liquid film (without subsequent floating bubble) was also observed in [72]. Furthermore, in this reference a correlation for the critical Weber number (We_{dry}) under which the centre of the drop dries out was proposed.

Evaluation of Eq. (10) predicts no dryout for Case B ($We_{\text{dry}} = 7.8 > We = 2.5$) and dryout for Case C ($We_{\text{dry}} = 7.4 < We = 11.7$) in agreement with the present results. For Case D it is by chance $We_{\text{dry}} = We = 7.5$. In the present simulation, dryout is observed for Case D.

The described bubble entrapment mechanism during recoil with or without drop rebound is confirmed by more recent experiments, see e.g. [78, 79] and references therein. Note that this mechanism is completely different from the bubble entrapment mechanism occurring in the very early stage of impact [80-82]. In the latter mechanism, the drop deforms as it approaches the wall and a dimple appears underneath due to compression of the ambient gas between the droplet and the surface [83]. After the initial contact is made, the air under the dimple is entrained and contracts into a bubble [84].

We close this validation by a remark concerning numerical accuracy. Achieving numerical convergence for drop impact simulation is a hard challenge because of moving contact-line dynamics and the small structures created by the impact [85]. We are not aware of any study where numerical convergence is proven for such complex impact dynamics as considered here and do not claim it for our study. However, the present simulations for Cases A-D accurately reproduce the overall experimental dynamics, while small deviations (thus as emission of a thin central jet) can be attributed to spatial resolution. As model parameter of the phase field method such as capillary width and mobility pre-factor have been kept fixed for the various cases, this good agreement points on the predictive capabilities of the phase field method for numerical simulation of drop rebound phenomena.
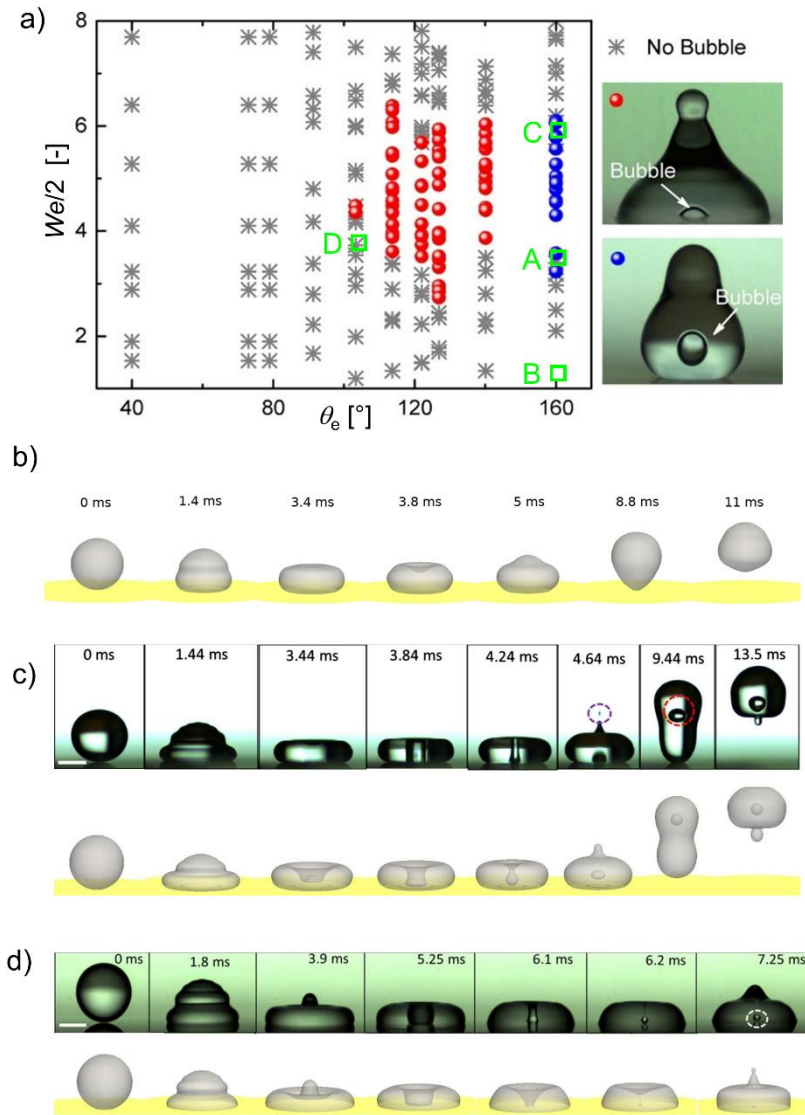
Figure 3: (a) Experimental regime map on bubble entrapment behaviour from ref. [74] with graphical legend displayed to the right. Star symbols: no optically detectable bubble; red bullets: bubble is attached to hydrophobic surface; blue bullet: bubble is floating in the drop bouncing from a superhydrophobic surface. Green open squares indicate the present simulation cases A-D. (b) – (d): Temporal evolution of droplet shapes ($D_0 = 2$ mm). b) Case B ($\theta_e = 161°$, $We = 2.5$, $Re = 665$). (c) Case C ($\theta_e = 161°$, $We = 11.7$, $Re = 1440$). (d) Case D ($\theta_e = 106°$, $We = 7.5$, $Re = 1152$). The upper rows of subfigures c) and d) show experiments of Lin et al. [70] (white scale bar = 1 mm) while the lower rows show present simulation results.

3.2 Contact time

In this section, we compare the contact time from numerical simulations with experimental results obtained for water drops impinging onto a superhydrophobic surface. In the experiments of Richard et al. [71], the initial drop diameter and impact velocity are varied between $0.2-8$ mm and $0.2-2.3$ m s^{-1} while the Weber number is in the range $0.3 \leq We \leq 37$. The value 0.2 mm is close to the upper range of UWS droplet diameters. Richard et al. [71] found the contact time being proportional to the inertia-capillary time scale following the scaling law

$$T_{\mathrm{ct}} = a_{\mathrm{ct}} \sqrt{\frac{\rho_{\mathrm{L}} D_0^3}{8\sigma}} \qquad (11)$$

The pre-factor was determined as $a_{\mathrm{ct}} = 2.6\pm0.1$. Notably, the contact time does not depend on the impact velocity.

In our simulations, we consider a superhydrophobic surface with contact angle $170°$ in combination with physical properties representative of water chosen as $\rho_{\mathrm{L}} = 1000$ kg m^{-3}, $\mu_{\mathrm{L}} = 1$ mPa s, $\sigma = 72$ mN m^{-1} in combination with $\rho_{\mathrm{G}} = 1.118$ kg m^{-3}, $\mu_{\mathrm{G}} = 1.82 \times 10^{-5}$ Pa s. Computations are performed for four distinct values of the drop diameter (100, 200, 400, 800 μm) and five distinct impact velocities (1, 1.5, 2, 2.5, 3 m s^{-1}) yielding Weber numbers in the range $1-100$ and Reynolds numbers in the range $100-2400$. Figure 4 displays the numerical contact times as evaluated from these 20 simulations as function of impact velocity. For each droplet size, T_{ct} is almost constant indicating that contact time does not depend on impact velocity in agreement with [71]. As the droplet diameter in the present simulation increases from 100 to 800 μm, the corresponding values of a_{ct} decrease from 2.74 to 2.32. They are in reasonable agreement with $a_{\mathrm{ct}} = 2.6\pm0.1$ obtained in [71] and the wider range $a_{\mathrm{ct}} = 1.6-3.2$ reported in [86] for various technical and natural substrates. Values of a_{ct} as low as 1.6 or even 1.25 [73] imply a significant reduction of contact time which is achieved by macro-texturing the superhydrophobic surface [86].
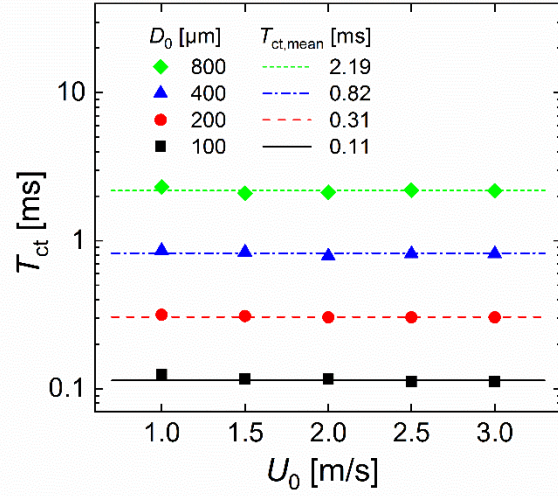
Figure 4: Contact time evaluated from numerical simulations with $\theta_e = 170°$ for four droplet diameters under five different impact velocities ($1 \leq We \leq 100$, $100 \leq Re \leq 2400$). The dashed lines represent the averaged contact time for each droplet size.

Figure 4 indicates that the contact time increases with increasing initial drop size. To analyze this relation quantitatively, Figure 5 displays the contact time as function of D_0, where numerical values for each diameter are averaged over the five impact velocities. As can be seen, the present numerical results from Figure 4 are in good agreement with the experimental data and correlation from Richard et al. [71]. The same holds for the present numerical results from Figure 2 (b) with $D_0 = 2$ mm. A similar increase of contact time with increase of diameter in the more narrow range 1.9 mm $\leq D_0 \leq 3$ mm is reported in [32].

In addition to the latter comparison with the experiment of Richard et al. [71], our investigation is extended to the influence of surface wettability on contact time. For that purpose, five additional simulations with drop diameter 200 μm and impact velocity 2 m s^{-1} are performed for contact angles 130, 140, 150, 160 and 180°. As demonstrated by the inset graphics in Figure 5, the contact time decreases from 0.375 to 0.3 ms as the equilibrium contact angle is increased from $130°$ to $180°$. This arises because as the solid becomes more hydrophobic, its energetic repellence against the water droplet gets stronger so that the contact time is shortened.
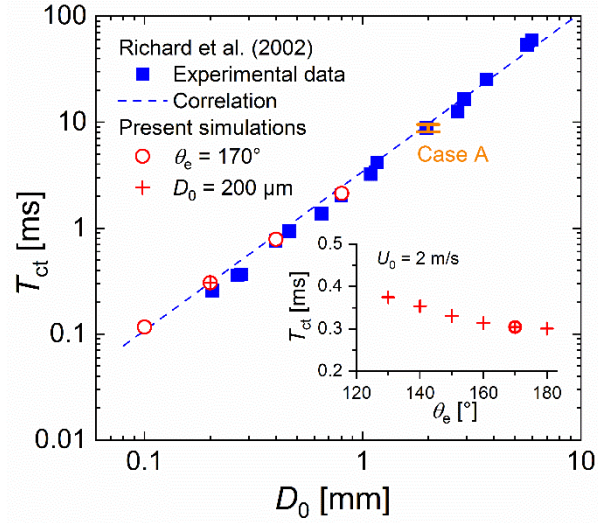
Figure 5: Contact time as function of initial droplet diameter: comparison of present numerical results (open circles) with experimental data (filled squares) [71]. The dashed line represents the scaling law of Eq. (11) with $a_{ct} = 2.6$ reported in [71]. The orange bar for $D_0 = 2$ mm shows the range of T_{ct} in the simulations for Case A, see Figure 2 (b). The inset shows the influence of contact angle on contact time for present numerical results ($D_0 = 200$ μm, $U_0 = 2$ m s^{-1}).

4   Impingement of UWS droplets

In this section, we study the normal impact of single UWS droplets on a flat horizontal surface numerically. The physical properties correspond approximately to those of AdBlue (a eutectic 32.5 wt% urea-water solution also named Diesel Exhaust Fluid) at atmospheric temperature and pressure ($\rho_L = 1090$ kg m^{-3}, $\mu_L = 1.526$ mPa s, $\rho_G = 1$ kg m^{-3}, $\mu_G = 1.82 \times 10^{-5}$ Pa s, $\sigma = 73.26$ mN m^{-1}) [87]. The ranges of investigated initial droplet diameter and impact velocity are chosen by consideration of typical hydrodynamic operating conditions in the exhaust gas tailpipe.

Liao et al. [43] investigated the spray characteristics of four commercially available UWS injectors under typical SCR conditions with temperature up to 300°C and maximum velocity of the gas cross-flow up to 26 m s^{-1}. In the experiments, water sprays were used since previous studies proved that the injected fluid water and AdBlue show similar behavior in terms of the bulk spray properties and droplet

size distribution [4]. Droplet sizes are typically in the range of $20-180$ μm [42], with Sauter mean diameter between $60-80$ μm for pressure-driven injectors and mean wall-normal velocities of the droplets up to 20 m s^{-1} [43]. Droplets larger than 90 μm have an increased probability to impinge on walls of the SCR system [42]. From the trailing edges of the mixer blades, however, drops up to millimetre size may be shed [88]. Thus, in the following simulations, the investigation range of the initial droplet diameter is $25-800$ μm and that of the impact velocity is $0.01 - 10$ m s^{-1}.

In recent experiments, equilibrium contact angles of sessile UWS droplets in the range $45° \leq \theta_e \leq 107°$ were measured on various substrates [7]. Here, the equilibrium contact angle is varied in the range $30-170°$. In terms of the three parameters D_0, U_0 and θ_e, the aim here is to identify conditions favorable to rebound occurrence. For this purpose, we first study the effects of these three parameters on the dynamic impact process. Thereafter, the maximum spread ratio is analyzed in detail. Finally, exploiting a large number of simulations, we present regime maps for deposition and rebound.

4.1 *Effects of single parameter variations on dynamic impact process*

The dynamics of the impact and spreading process is usually characterized by the spread ratio. The time evolution of the spread ratio $\beta = \beta(t)$ can be described as a sequence of four distinct phases: kinematic, spreading, relaxation and wetting/equilibrium [89]. In this section, we study the influence of variation of one parameter of the set (θ_e, U_0, D_0) on $\beta = \beta(t)$ while keeping the two other parameters fixed.

4.1.1 *Influence of equilibrium contact angle*

To study the influence of wettability on the impact process, simulations with fixed droplet diameter and impact velocity are performed. The chosen droplet size of 68.3 μm represents a typical Sauter mean diameter of industrial pressure-driven UWS injectors [43, 90]. A typical injection velocity in SCR systems is 27 m s^{-1} [91] while typical spray velocities are about 20 m s^{-1} [90]. In practice, the UWS spray is injected with a certain inclination angle with respect to the flow direction, e.g. 50° in [91]. The wall-normal component of the drop velocity at impact is therefore much smaller than

20 m s^{-1}. As in this study the normal axisymmetric impact of a single UWS droplet is considered for simplicity, the impingement velocity is set arbitrarily to 7.23 m s^{-1}. These conditions correspond to $We = 53.1$, $Re = 352.6$ and $Oh = 0.021$.

The simulations encompass six different values of the equilibrium contact angle, namely 30, 65, 100, 120, 135, and 170°. The corresponding temporal evolutions of the spreading ratio are shown in Figure 6. The individual behaviour of $\beta = \beta(t)$ is governed by a competition between three forces (inertia, surface tension, viscosity) and associated energies. At the very beginning ($t \leq 10$ µs), the equilibrium contact angle θ_e exhibits almost no effect on the spreading process, since during this initial stage inertial effects largely dominate over capillary effects so that the influence of wettability is negligible. After this very short kinematic phase, the subsequent spreading, relaxation and wetting/equilibrium phases are strongly affected by wettability.

For all contact angles displayed in Figure 6, inertia causes the droplet to spread beyond the equilibrium state. The maximum spread factor β_{max} and the time t_{max} of maximum spreading decrease with increase of θ_e. At maximum spreading, a part of the initial kinetic energy is already dissipated by viscosity. The energy loss during the advancing phase of spreading increases with β_{max} and thus decreases with increase of θ_e. The difference between surface energy at maximum spreading and the equilibrium state causes the droplet to recoil for $t > t_{\mathrm{max}}$. Figure 6 shows that recoil is strongly affected by the contact angle and two cases can be distinguished. In the case of deposition ($\theta_e \leq 100°$), the spread factor approaches a finite terminal value corresponding to partial wetting conditions, whereas in the case of rebound ($\theta_e \geq 120°$) the spread factor becomes zero at $t = T_{\mathrm{ct}}$.

Even for droplets undergoing deposition, the recoil process is greatly affected by wettability [92] as it depends on the amount of excess surface energy which increases with increase of θ_e. If excess surface energy is relatively low (as is the case for contact angles 30° and 65°), the recoil process is smoothly with a monotonic decrease of the spreading factor toward the equilibrium spread ratio β_∞. The time required to reach the final equilibrium spread ratio β_∞ is very short for $\theta_e = 30°$, as β_{max} is only slightly larger than β_∞, but increases for $\theta_e = 65°$. If the excess surface energy is higher, the recoil process is faster (the slope of β in Figure 6 increases with θ_e) and inertia causes the spreading factor to

decrease below the equilibrium value. In the case with $\theta_e = 100°$, the motion of the receding contact line slows down and eventually stops so that a relative minimum of β is reached at $t \approx 72$ms. Thereafter, β increases again causing an oscillation around the equilibrium spreading factor. This oscillation is damped in time by viscous forces. This oscillation is in agreement with experimental observations. As noted by Kim and Chun [92], droplet deposition on a poor wetting substrate ($\theta_e = 87.4°$) gives rise to oscillations of the wetted area before the equilibrium sessile form is reached. For the UWS simulations, the value of the Bond number $Bo = g(\rho_L - \rho_G)D_0^2/\sigma$ is always below 0.1. Therefore, gravitational effects are negligible. Accordingly, droplets undergoing deposition adopt a terminal equilibrium shape in form of a truncated sphere. As in [52], the computed terminal spread factor in the present simulations is in good agreement with the analytical spread factor of a spherical cap [89, 93].

For contact angles 120° and above, the excess surface energy is sufficiently large to cause drop rebound off the solid surface at the end of the receding phase. As the equilibrium contact angle increases further, the rebound occurs earlier decreasing the contact time T_{ct}. This trend matches with the results displayed in the inset of Figure 5. In addition, larger equilibrium contact angles result in a smaller maximum spreading ratio. Thus, the area wetted during drop impact gets smaller, reducing the chance of film formation.
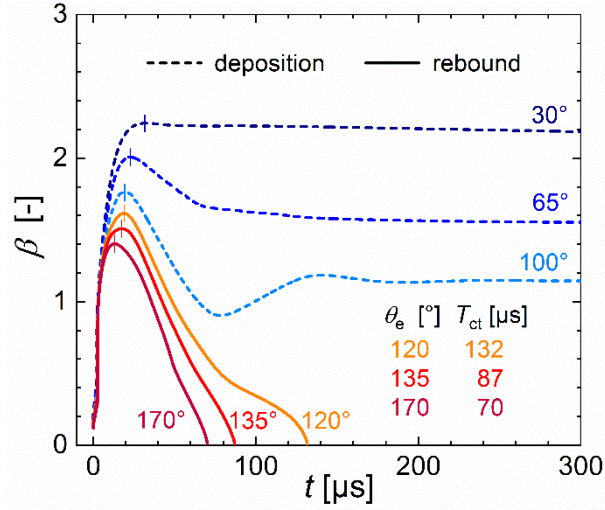
Figure 6: Influence of contact angle on dynamic droplet impact process for fixed values of droplet diameter and impact velocity ($D_0 = 68.3$ μm, $U_0 = 7.23$ m s^{-1}, $We = 53.1$, $Re = 352.6$, $Oh = 0.021$). The small vertical bars indicate t_{max}, i.e., the instant in time for which the spreading ratio attains its maximum value β_{max}.

4.1.2   *Influence of impact velocity*

To study the influence of impact velocity, the droplet diameter is again fixed to 68.3 μm while the equilibrium contact angle is set to 130°. Six distinct values of the impact velocity in the range $0.1 - 10$ m s^{-1} are considered corresponding to $0.01 \le We \le 102$ and $4.9 \le Re \le 488$ and constant Ohnesorge number $Oh = 0.021$. Figure 7 shows that a variation of the impact speed affects the entire impact process from the very beginning. For $U_0 \le 1$ m s^{-1} the droplet spreads out and deposits on the surface while for $U_0 \ge 1.5$ m s^{-1} rebound occurs. For bouncing droplets, the contact time T_{ct} is notably affected by the impact velocity in a non-monotonic manner. The observed dependence of T_{ct} on U_0 in Figure 7 deviates from the findings in Section 3.2, where the contact time shows, at least in the semi-logarithmic representation of Figure 4, almost no dependence on impact velocity. There are two potential reasons to explain this contrasting behavior: the different contact angles (130° versus 170°) and the differences in Reynolds number. While the range of We is similar, the range of Re in this

section is much smaller than that studied in Section 3.2. Thus, viscous effects are much more important here so that the scaling by the inertia-capillary time scale found in Eq. (11) may not be valid.
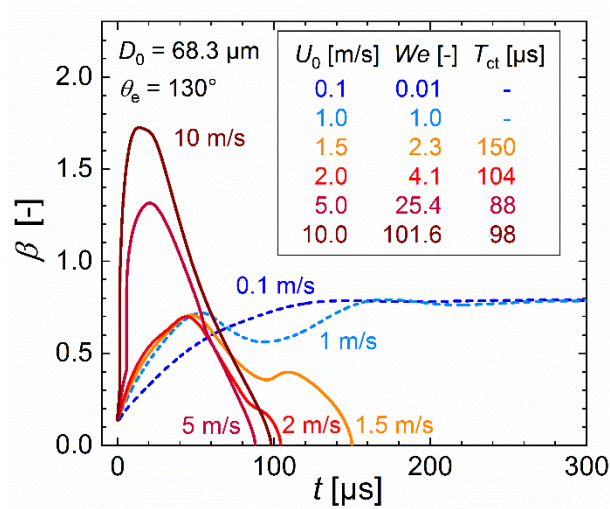
Figure 7: Effect of impact velocity on spreading ratio for fixed values of droplet diameter and contact angle ($D_0 = 68.3$ µm, $\theta_e = 130°$, $Oh = 0.021$, $4.9 \leq Re \leq 488$).

4.1.3 Influence of droplet diameter

To study the effect of droplet size, simulations for drop diameters of 100, 200, 400, and 800 µm are performed with fixed impact velocity (5 m s^{-1}) and equilibrium contact angle (130°). With increase of drop diameter, the Ohnesorge number decreases from 0.017 to 0.006. As Figure 8 shows, a smaller droplet reaches its maximum spread factor β_{max} earlier, yet the value of β_{max} is lower than that of a larger droplet. With larger D_0, the contact time increases; this agrees with the previous results in Figure 5. For diameter values 400 µm and below, the spread factor gradually approaches to zero before the droplet rebounds from the solid wall. However, for diameter 800 µm, the spread factor suddenly jumps to zero at $t \approx 1.64$ ms. This is related to an air film formed below the drop as the drop impinges the surface, similar to case A with $Cn = 0.01$. Whether the droplet punctures the air film or

26

not during spreading on a real surface, is likely to depend on surface roughness [93]. As the solid surface in the present simulations is ideally smooth, the air layer persists.

The results of Figs. $6 - 8$, where one of the parameters (θ_e, U_0, D_0) is varied while the other two are fixed, can be summarized as follows. The time of maximum spreading (t_{max}) decreases with equilibrium contact angle and impact velocity but increases with drop diameter. Thus, opposite trends on the dependence of t_{max} on We are observed in Figure 7 and Figure 8. The maximum spreading ratio (β_{max}) decreases with contact angle and drop diameter but increases with impingement velocity. In the next subsection, results for the maximum spread ratio will be compared in a quantitative manner.
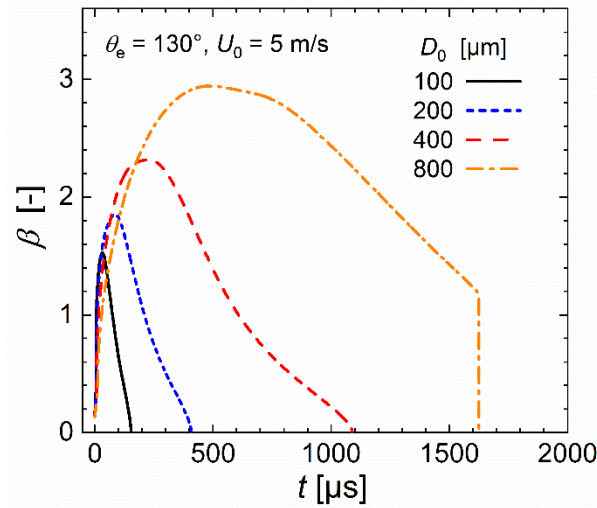
Figure 8: Influence of drop diameter on dynamic rebound process for fixed values of impact velocity $(U_0 = 5 \text{ m s}^{-1})$ and contact angle ($\theta_e = 130°$).

4.2 Maximum spreading ratio

During the impact process, the droplet initially spreads out until it reaches a maximum diameter. Thereafter, the drop recoils resulting either in deposition or bouncing. In this subsection, we discuss results for the maximum and terminal spreading ratio for non-bouncing droplets undergoing deposition. The maximum spreading ratio $\beta_{max} = \beta(t_{max})$ of non-bouncing droplets is of particular interest here, as coalescence of neighboring impinging droplets may initiate UWS film formation. Additionally, the

size of the wetted area affects the evaporative cooling of the wall. If β_{max} can be reduced, the probability of droplet interaction and UWS liquid film formation might decrease. The knowledge of β_{max} is also of interest for predicting bouncing. Mao et al. [26] e.g., proposed a model that predicts the tendency to rebound as a function of maximum spread and static contact angle.

Spreading is governed by the balance between kinetic, gravitational and surface energy of the drop, in combination with the energy loss due to viscous dissipation. Therefore, energy balance approaches are commonly used to predict maximum spreading or rebound conditions theoretically [26, 94-101]. A main difficulty of such simplified models is the adequate modelling of dissipation [100]. While dissipation during drop impact can hardly be quantified experimentally, it is amenable by direct numerical simulation [102]. In addition to energy-based models, simplified theoretical models based on force balances or mass and momentum equations are quite common [103, 104].

For predicting the maximum spreading ratio β_{max}, several correlations and relationships have been proposed. Studies in the literature have reported scaling laws for the viscous regime ($\beta_{max} \propto Re^{1/5}$) [105] and the capillary-inertial regimes ($\beta_{max} \propto We^{1/2}$ or $We^{1/4}$) [23, 106]. However, the applicability of scaling laws is often limited to certain liquids and that of empirical correlations to certain experimental ranges. Lee et al. [102] for example found that the scaling of maximum spread ratio as suggested by Clanet et al. [106], although predicting the behavior for water, does not predict maximum spreading for ethanol and glycerol droplets. Börnhorst et al. [52] recently compared experimental and numerical data for the maximum spread ratio of UWS droplets impacting on a hydrophilic surface ($\theta_e = 50.3°$) with the empirical correlation $\beta_{max} = 0.62(Re^2 Oh)^{0.166}$ proposed by Scheller & Bousfield [103]. For millimetre-size UWS droplets and moderate impact velocities comparable to the experimental conditions in [103] with droplets consisting of glycerol-water-ethanol mixtures, good agreement was obtained. A numerical simulation for a much smaller droplet, however, indicated that this correlation for β_{max} is not valid for submillimetre-size droplets of UWS sprays in technical applications [52]. No consensus on which formulation should be used under which conditions has been reached so far and the quantitative prediction of β_{max} for a wide range of We (or Re) is a challenging problem. Lin et al. [70], e.g., note that none of the existing theoretical models can well

describe the maximum spreading ratio observed in their experiments. Accordingly, improved empirical models are developed for certain liquids [107].

Figure 9 shows the maximum spreading ratio as a function of Weber number for the simulations from Section 4.1. To investigate the influence of surface wettability on maximum spread factor in more detail, the figure is supplemented by simulation results for contact angles 52° and 100°. Similar to Section 4.1.3, the impact velocity is fixed ($U_0 = 7.23$ m s^{-1}). The set of initial UWS droplet diameters is 25, 50, 100 and 200 µm. The corresponding ranges of the Weber, Reynolds, and Ohnesorge numbers are 19.4–155.5, 129–1033, and 0.012–0.034, respectively.

From impact experiments with millimetre-sized droplets, Antonini et al. [108] identified two regimes: a moderate Weber number regime ($30 < We < 200$), in which wettability affects both drop maximum spreading and spreading characteristic time, and a high Weber number regime ($We > 200$), in which wettability effect is secondary, because capillary forces are overcome by inertial effects. With exception of the simulation with $D_0 = 800$ µm where $We = 297.6$, all present cases for sub-millimetre UWS droplets belong to the low Weber regime. In agreement with [108], a notable influence of wettability is identified in Figure 9. For fixed U_0 and D_0, an increase of θ_e results in a decrease of β_{max}, cf. Section 4.1.1. For fixed U_0 and θ_e, an increase of D_0 results in a strong increase of β_{max}, cf. Section 4.1.3. Notably, the scenarios with fixed parameters ($\theta_e = 100°$, $U_0 = 7.23$ m s^{-1}) and ($\theta_e = 130°$, $U_0 = 5$ m s^{-1}) have almost the same values of β_{max} over the entire Weber number range. The comparison of cases for $\theta_e = 130°$ where either $U_0 = 5$ m s^{-1} or $D_0 = 68.3$ µm is fixed is also interesting, as in the Weber number range $25 - 100$ values of β_{max} do not collapse on a single curve. This shows that β_{max} does not only depend on Weber number but also on Reynolds number. The scaling with Weber number is illustrated by two power laws in Figure 9. For simulations where the impact velocity U_0 is fixed and where the Weber number varies due to change of D_0, the power law exponent is between 0.25 and 0.5, in agreement with scaling laws proposed in literature. The scaling $\beta_{max} \propto We^{1/2}$ arises under the assumption that the kinetic energy in the drop is converted to surface energy [72]. This implies that dissipation is negligible, which is not realistic here where in most cases very small droplets are impinging with high velocity.
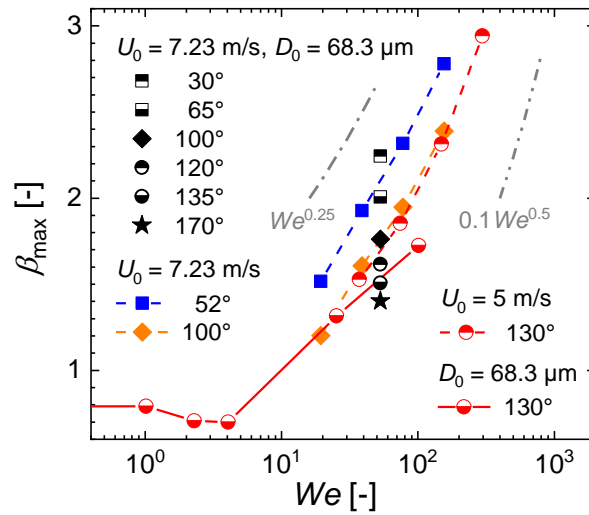
Figure 9: Numerical results for maximal spread factor of UWS droplets as function of We. Black symbols (without line) correspond to Figure 6 where both D_0 and U_0 are fixed. Symbols connected by dashed lines correspond to cases where D_0 is varied while U_0 is fixed. Symbols connected by solid lines correspond to cases where U_0 is varied while D_0 is fixed.

4.3 Drop rebound regime maps

In this subsection, numerical regime maps for bouncing/non-bouncing droplets are presented. As rebound is governed by an inertia-capillary interplay, the Weber number plays a prominent role in predicting conditions for bouncing. Mao et al. [26] derived a semi-empirical model for rebound criteria as an implicit function of equilibrium contact angle, Weber number and Reynolds number. This model is valid when both We and Re are relatively high.

Caviezel et al. [35] derived a criterion for drop adherence, respectively rebound, by considering the difference in surface energy before impact (where the drop is spherical) and at equilibrium (where the drop adheres to the surface in the form of a spherical cap). By this approach, the critical Weber number for rebound $We_{cr} = \rho_L D_0 U_{cr}^2 / \sigma$ depends on equilibrium contact angle θ_e as

$$We_{cr} = 12\left\{1 - \frac{2 - 3\cos\theta_e + \cos^3\theta_e}{[2(1 - \cos\theta_e)(2 - \cos\theta_e - \cos^2\theta_e)]^{2/3}}\right\} \tag{12}$$

(see Supplemental Material B and [109]). The model is claimed to be valid for small We (when surface tension effects dominate inertia) and moderate Re, as viscous dissipation is neglected.

30

Reyssat et al. [27] argued that drop rebound on a superhydrophobic surface happens when the drop kinetic energy is larger than its surface energy, so the critical impact velocity to observe rebound is

$$U_{cr} \sim \sqrt{\frac{\sigma}{\rho_L D_0}} \, . \tag{13}$$

The pre-factor in Eq. (13) quantifies the effect of contact angle hysteresis [27], which we do not account for here. The relation in Eq. (13) can be expressed in terms of a critical Weber number $We_{cr} = \rho_L D_0 U_{cr}^2/\sigma$. Rioboo et al. [110] performed drop impact experiments on a porous superhydrophobic polymer surface and determined a quantitative relation for We_{cr} in terms of advancing and receding contact angles. More recently, Bange [40] derived by numerical simulations a regime map in $We - Re$ space to predict the bouncing and non-bouncing droplets on a superhydrophobic surface ($\theta_e \approx 155°$). For a given liquid such as UWS, such a regime map is of limited use since it is not possible to vary We and Re independently. In the following we therefore show regime maps mainly in terms of dimensional parameters.

Results from Section 4.1 have shown that drop diameter, drop impact velocity and contact angle are important parameters determining whether droplet bouncing occurs or not. In order to clarify the effects, a large number of simulations are carried out and three maps for deposit and rebound regimes are formulated based on these parameters.

First, the combined effects of the equilibrium contact angle and initial droplet diameter on the deposit/rebound regimes are studied. With θ_e being varied from 60° to 120° and D_0 from 50–400 μm, a series of numerical simulations for a fixed impact velocity (7.23 m s^{-1}) are carried out. As presented in Figure 10, droplets deposit for $\theta_e \leq 75°$ and rebound for $\theta_e \geq 110°$, irrespectively of initial diameter. A transition region exists within the range $75° < \theta_e < 110°$, where a dependence of droplet deposit/rebound or partial rebound behavior on θ_e and D_0 is observed. For partial rebound, the drop does not have enough kinetic energy to rebound completely from the surface in recoil stage. Thus, in the interaction of different forces acting on droplet including capillary, inertia forces and gravity, a neck forms in the upper part of the droplet, which narrows over time and eventually breaks, splitting the droplet into two parts. The upper daughter droplet bounces off while the lower one deposits on the

surface. From Figure 10 it can be seen, that for a given droplet diameter an increase of θ_e results in a transition from deposition to partial rebound and complete rebound. For droplet sizes $D_0 \leq 100$ µm, the partial rebound occurs over a range of θ_e of about $20 - 30°$. For droplet sizes $D_0 \geq 200$ µm, this range is only about $10 - 20°$. For $D_0 = 50$ µm droplets, complete rebound is obtained for $\theta_e \geq 110°$, whereas for droplet sizes $D_0 \geq 100$ µm it is obtained for $\theta_e \geq 95°$. An exception is drop diameter $D_0 = 400$ µm, where complete rebound is observed already for $\theta_e = 90°$. However, it is important to remark that in the transition region with partial rebound, results on impact outcome have to be interpreted with care since the pinch-off process leading to drop splitting is likely to depend on Cahn number. In the following regime maps, partial rebound will not be considered separately, but will be attributed to deposition regime.
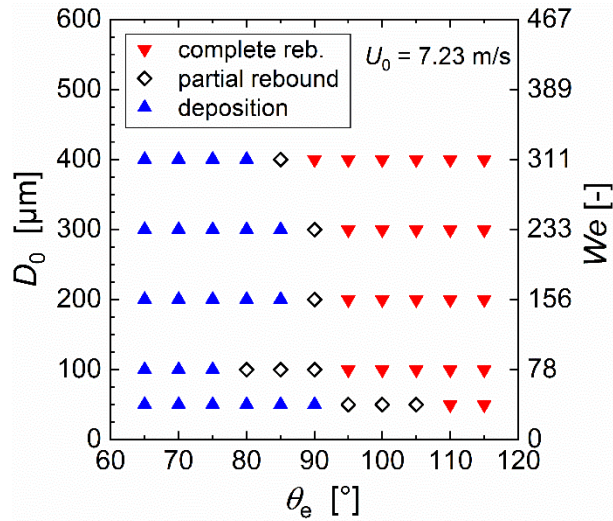
Figure 10: Outcomes of numerical impingement events under variation of drop diameter and equilibrium contact angle. $D_0 - \theta_e$ regime map for $U_0 = 7.23$ m s^{-1}.

Figure 11 presents a regime map in terms of impact velocity and equilibrium contact angle. With fixed droplet diameter (68.3 µm), θ_e and U_0 are systematically varied in the ranges $80 - 170°$ and $0.01 - 10$ m s^{-1}. As shown in Figure 11, when $\theta_e < 120°$ the droplet will deposit on the wall for all the investigation range of the impact velocity. On the other hand, for $\theta_e > 150°$ the droplet rebounds irrespective of the value of U_0. A dependence of rebound versus non-rebound behavior on U_0 is only

observed for the contact angle range $120° \leq \theta_e \leq 150°$. As θ_e increases within this range, the threshold impact velocity for achieving rebound decreases. This can be explained by the dependence of β_{max} and t_{max} on θ_e for fixed diameter and impact velocity: as θ_e increases, both β_{max} and t_{max} decrease, cf. Figure 6. Accordingly, less of the drop's initial kinetic energy is dissipated with increase of θ_e during the advancing phase of spreading ($t < t_{max}$). If kinetic energy is assumed approximately zero at $t = t_{max}$, and if dissipation during recoil is considered negligible, then with increase of θ_e more of the initial kinetic energy is available in the late phase of recoil. Therefore, with increase of θ_e, droplets of given diameter rebound at lower U_0, as observed in Figure 11 for the range $120° \leq \theta_e \leq 150°$.

In Figure 11, the Weber number criterion from Eq. (12) is plotted for the range $90° \leq \theta_e \leq 150°$. The curve shows the same qualitative trend as the numerical simulations: as the contact angle increases, a smaller critical Weber number is needed for rebound occurrence. Quantitatively, the critical Weber number obtained by the simulations is larger than predicted by Eq. (12). This is reasonable as in the derivation of Eq. (12) viscous dissipation has been neglected.
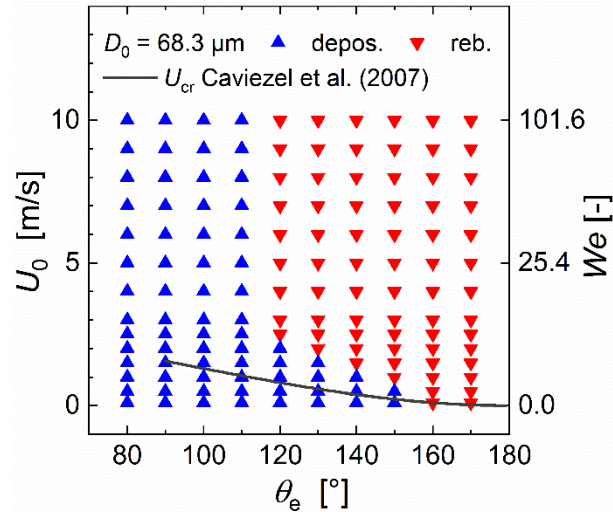
Figure 11: Outcomes of numerical impingement events under variation of impact velocity and equilibrium contact angle. $U_0 - \theta_e$ regime map for $D_0 = 68.3$ µm ($Oh = 0.021$). The solid line corresponds to the adherence criterion of Caviezel et al. [35] given by Eq. (12).

Figure 12 illustrates the rebound – no-rebound behavior on the $U_0 - D_0$ plane. While the initial

drop diameter and impact velocity are varied in the ranges $25 - 800$ μm and $0.5 - 10$ m s^{-1},

respectively, the equilibrium contact angle is kept fixed at $\theta_e = 130°$. It is evident that as the droplet

size increases, the critical impact velocity to achieve rebound decreases. On the log-log scale, a plot of

relation (13) results in a straight line with slope $-1/2$. The corresponding deposition/rebound criterion

for $We_{cr} = 3$ is displayed in Figure 12 as black solid line; it describes the demarcation of the

impingement outcomes in the present simulations for $\theta_e = 130°$ reasonably well. As additional

information, the fill colour of the symbols in Figure 12 indicates the Reynolds number. Accordingly, a

rebound is always observed for Reynolds numbers larger than 200.
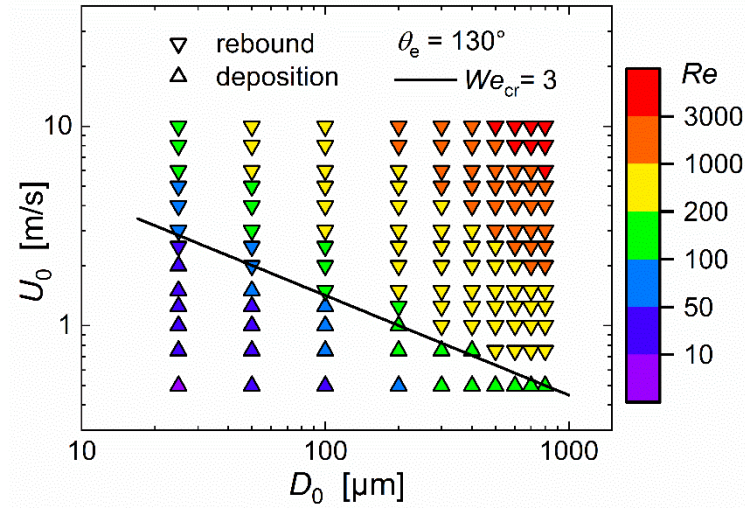
Figure 12: Outcomes of numerical impingement events on a smooth hydrophobic surface ($\theta_e = 130°$) under variation of drop diameter and impact velocity.

4.4 Maximum bounce height

The regime maps presented in the previous subsection indicate if rebound is observed in the

simulation or not. To quantify rebound, in this subsection the maximum rebound (bounce) height h_{reb}

is considered, which is defined as the maximum vertical distance between the surface and the bottom of

the bouncing drop. Experimental results for water droplets of size $D_0 = 1.97$ mm show that h_{reb} increases with Weber number [111]. Even for the smallest Weber number ($We = 9$) considered in that study, the normalized maximum bounce height takes a value of $h_{\text{reb}}/D_0 \approx 3.7$ for an initially spherical droplet. For micrometre droplets, no experimental data for h_{reb} are reported in literature to our knowledge.

To study maximum bounce height, additional simulations for UWS drop impact on a hydrophobic surface ($\theta_e = 130°$) have been performed for nine distinct drop diameters in the range $50 - 800$ μm and impact velocities in the range $0.2 - 0.7$ m s^{-1}. The simulations have been performed with reduced Cahn number $Cn = 0.01$ and $\chi = 1$ m s kg^{-1}. The dimensions of the computational domain are $W/D_0 = 1.75$ and $H/D_0 = 2.75$. The impact velocities are kept relatively low in order to keep rebound height limited, so that the droplet stays always inside the computational domain. While in previous sections, simulations have been stopped shortly after rebound, the simulations here are continued over an extended time until the bouncing drop begins falling downward again due to gravity.

Figure 13 displays the normalized maximum rebound height h_{reb}/D_0 over the $U_0 - D_0$ plane. Within this plane, the solid line indicates $We_{\text{cr}} = 3$ which was found to be good discrimination for the regimes in Figure 12. Here, it serves less well for indicating rebound. For comparison, $We_{\text{cr}} = 1$ is included as dashed line. Appreciable values of the relative rebound height $h_{\text{reb}}/D_0 > 0.1$ are only observed for impact velocities $U_0 \geq 0.4$ m s^{-1} regardless of droplet diameter. For a fixed droplet diameter, the relative rebound height increases with impact velocity as expected. For fixed impact velocities $U_0 > 0.5$ m s^{-1}, the normalized rebound height h_{reb}/D_0 increases as the drop diameter increases from 50μm to 400 μm. This behaviour may be related to the fact that with increased drop diameter, a lower fraction of liquid volume is within the viscous boundary layer. Therefore, one may expect the viscous dissipation being relatively lower for larger drops given the same impact velocity. However, with further increase of D_0, the relative rebound height decreases again. Now we have no explanation for this behaviour. We point out that results for the rebound height must be considered preliminary and the reported findings have to be interpreted with care.
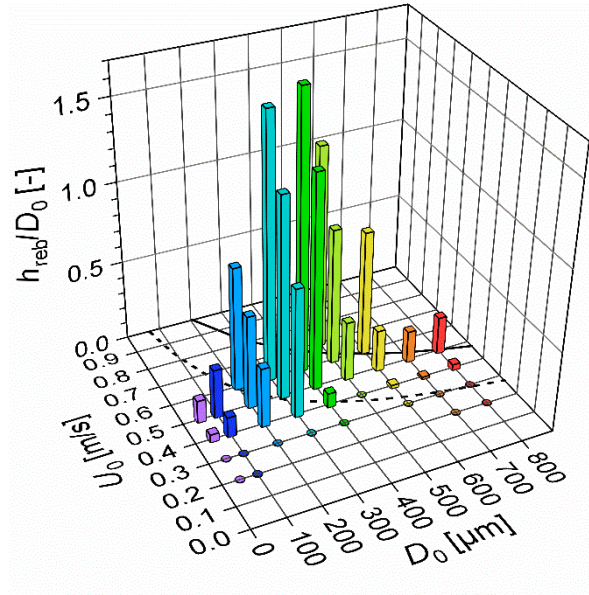
Figure 13: Normalized maximum rebound height h_{reb}/D_0 from a hydrophobic surface ($\theta_{\mathrm{e}} = 130°$) for various combinations of drop diameter and impact velocity. Square columns indicate cases with rebound while cases without rebound are marked by circles. Colours serve to distinguish different droplets diameters. The solid and dashed lines indicate critical Weber numbers of 3 and 1, respectively.

5   Summary and conclusions

In the first part of this paper, a phase-field method has been thoroughly validated for impact and rebound of millimetre-sized water droplet on hydrophobic surfaces. Numerical results for instantaneous droplet shape, spread factor and contact time obtained by axisymmetric computations have been compared against experiments from literature showing good agreement in general. However, a slight influence of numerical parameters such as thickness and resolution of the diffuse interface on maximum spreading and contact time has to be noted.

In the second and main part of the paper, a comprehensive numerical study on the impact dynamics of urea-water-solution (UWS) droplets on substrates of varying wettability (equilibrium contact angle $30° \leq \theta_{\mathrm{e}} \leq 170°$) has been performed. The axisymmetric simulations cover a wide range of sub-millimetre droplet sizes ($25\ \mu\mathrm{m} \leq D_0 \leq 800\ \mu\mathrm{m}$) at various impact speeds ($0.01\ \mathrm{m\ s^{-1}} \leq U_0 \leq$

10 m s^{-1}), corresponding to typical hydrodynamic operating conditions in exhaust after-treatment, albeit under isothermal ambient conditions. In terms of relevant non-dimensional groups, simulation results cover maximum values of Weber number and Reynolds numbers of about 300 and 2900, respectively. These numerical simulations are unique as, to the knowledge of the authors, no experimental data for impingement behaviour of single sub-millimetre UWS droplets are available in literature. However, the good agreement obtained between numerical predictions and millimetre-scale experiments does not mean that the numerical results obtained by the code for the submillimetre scale are valid without restriction. Factors that are not included in the model are evaporation, roughness and inhomogeneity of the surface and the potential presence of any surface-active substances. While these factors might already effect phenomena at millimetre scale, they become more and more important for smaller length scales, until ultimately the line tension matters as well [112].

Trends identified in the numerical simulations for UWS droplets follow the behaviour observed for water droplets of mm-size. After the initial kinematic phase, a strong influence of wettability on droplet dynamics is identified. The maximum spreading ratio (β_{max}) decreases with contact angle and drop diameter but increases with impingement velocity. For β_{max}, no consistent scaling in terms of Weber number could be identified, indicating that Reynolds number and Ohnesorge number are important too. A further focus of the present study was identifying conditions where UWS droplets rebound from the surface after first contact. As for other liquids, the key for obtaining rebound is hydrophobicity of the surface. A notable rebound for a wide range of droplet sizes and impact velocities is obtained only for equilibrium contact angles $\theta_{\mathrm{e}} \geq 120°$. On such hydrophobic surfaces, increase of droplet size and impact velocity favors rebound. A rebound criterion in terms of a critical Weber number of about 3 has been found to describe the impact outcomes of numerical simulations reasonably well. The present results may be useful for development of more advanced drop-wall interaction models as they are required in CFD codes relying on the Euler-Lagrange approach for engineering computations of UWS sprays.

The findings of the present fundamental study give useful hints for improvement of technical SCR systems relying on injection of UWS. Even if contact angles $\theta_{\mathrm{e}} \geq 120°$ may not be realized in

tailpipes, changing the contact angle by surface treatment from about 50° (which is a representative value for today's exhaust pipe materials) towards 90° may still significantly reduce maximum spreading. Thereby, local cooling of the exhaust pipe wall and liquid formation due to coalescence of droplets impinging at neighboring sites are reduced. The reduction of both effects may contribute to minimize or avoid the formation of solid deposits impairing exhaust after-treatment.

The present study was limited to the normal impact of single droplets under axisymmetric conditions without splashing. Next, the interaction of multiple UWS droplet impinging on a dry or pre-wetted wall will be investigated. Furthermore, the numerical method is currently extended towards conjugate heat transfer between droplet and solid wall.

Acknowledgement

Appendix

In this Appendix, the contact angle during spreading and recoil process is illustrated for drop impact on a hydrophobic surface. The parameters of the simulation are selected so that the deviation of the actual contact angle from the equilibrium contact angle can be readily visualized and recognized. The drop diameter $D_0 = 2.1$ mm, the impact velocity $U_0 = 0.61$ m s^{-1} and the fluid properties are similar to those of Case C, while the equilibrium contact angle is set to $\theta_e = 120°$. Furthermore it is $Cn = 0.02$ and $N_{di} = 6$ for this case.

Figure 14 presents droplet profiles (thick lines) at representative time instants covering the advancing phase (blue and light blue line) and the receding phase (orange and red line). The dark-grey curve shows the droplet shape at the time of maximum spreading ($t_{max} = 4.42$ ms). The thin straight black lines in Figure 14 illustrate the equilibrium contact angle $\theta_e = 120°$. Shortly after maximum spreading, at $t = 5.32$ ms, the drop shape is similar to a "pancake" with uniform thickness in the center and a thickened outer toroidal rim. The thickness of the pancake corresponds to the height where the drop surface first collides with the boundary layer where the radial flow created by impact adjusts to the no-slip condition at the wall [113]. After that instant in time, surface tension causes the drop to retract inwards.

The time instants $t = 1.12$ ms and $t = 9.60$ ms are selected because the contact line has the same radial position. For each of these two instants in time, the inset in Figure 14 shows a zoom-in of the local region near the contact line. During the advancing phase ($t = 1.12$ ms) when the contact line moves with high speed, the contact angle is notably larger than the equilibrium value $\theta_e = 120°$ adopted in the receding phase ($t = 9.60$ ms). This result confirms the findings in [54] that in phase-field methods employing the equilibrium contact angle as a boundary condition, cf. Eq. (5), the actual contact angle in the simulation may nevertheless deviate from this equilibrium value. The dependence of contact angle on contact line speed resembles a dynamic contact angle model. However, so far the detailed relation between contact angle and contact line speed has not been explored for our code. Accordingly, the dynamic contact angle is more an implicit feature and not comparable to dynamic

contact angle models in other approaches, where an explicit relation between dynamic contact angle and contact line speed is prescribed.
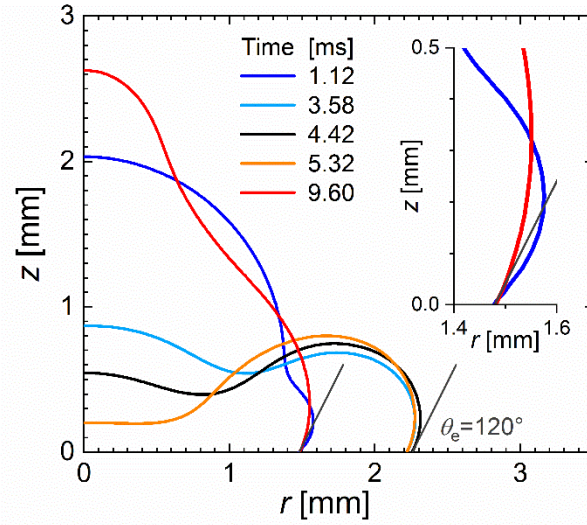
Figure 14: Droplet shape and apparent contact angle during different stages of the impact process. The time of maximum spreading is $t_{max} = 4.42$ ms. The figure also illustrates that for impact on hydrophobic surfaces the maximum radial dimension of the drop can be larger than the maximum wetted radius.

Nomenclature

Bo	Bond number (–), $Bo = g(\rho_L - \rho_G)D_0^2/\sigma$
C	order parameter (–)
Cn	Cahn number (–)
D_0	initial drop diameter (m)
D_{wet}	diameter of wetted circular area (m)
$\mathbf{g}$	gravity vector (m s^{-2})
g	gravitational acceleration (m s^{-2})
h	mesh size (m)
H	height of computational domain (m)
H_θ	contact angle hysteresis (°)
M	mobility (m^3 s kg^{-1})
$\mathbf{n}_s$	unit normal vector to the solid surface (–)

N_{di}	number of mesh cells across diffuse interface
Oh	Ohnesorge number (−), $Oh = \mu_L / \sqrt{\rho_L \sigma D_0}$
p	pressure (N m^{-2})
r	radial coordinate (m)
Re	Reynolds number (−), $Re = \rho_L D_0 U_0 / \mu_L$
t	time (s)
T_{ct}	contact time (s)
U_0	drop impact velocity (m s^{-1})
$\mathbf{u}$	velocity field (m s^{-1})
W	width of computational domain (m)
We	Weber number (−), $We = \rho_L D_0 U_0^2 / \sigma$
z	vertical coordinate (m)

Greek symbols

β	spreading ratio (−)
ε	capillary width (m)
λ	mixing energy parameter (J m^{-1})
μ	dynamic viscosity (Pa s)
ϕ	Cahn-Hilliard chemical potential (J m^{-3})
ρ	density (kg m^{-3})
σ	coefficient of surface tension (N m^{-1})
θ_a	advancing contact angle (°)
θ_e	equilibrium contact angle (°)
θ_r	receding contact angle (°)
χ	pre-factor in mobility relation (m s kg^{-1})

Subscripts

0	initial value
G	gas phase
L	liquid phase
max	maximum value

References

[1] I. Nova, E. Tronconi, Urea-SCR technology for deNOx after treatment of diesel exhausts, Springer, New York, 2014.

[2] B. Guan, R. Zhan, H. Lin, Z. Huang, Review of state of the art technologies of selective catalytic reduction of NOx from diesel engine exhaust, Appl. Therm. Eng., 66 (2014) 395-414.

[3] M. Koebel, M. Elsener, M. Kleemann, Urea-SCR: a promising technique to reduce NO_x emissions from automotive diesel engines, Catal. Today, 59 (2000) 335-345.

[4] A. Spiteri, P. Dimopoulos Eggenschwiler, Experimental Fluid Dynamic Investigation of Urea–Water Sprays for Diesel Selective Catalytic Reduction–DeNOx Applications, Ind. Eng. Chem. Res., 53 (2014) 3047-3055.

[5] F. Birkhold, U. Meingast, P. Wassermann, O. Deutschmann, Analysis of the Injection of Urea-Water-Solution for Automotive SCR DeNO$_x$-Systems: Modeling of Two-Phase Flow and Spray/Wall-Interaction, SAE Technical Paper 2006-01-0643, (2006).

[6] D. Schweigert, B. Damson, H. Lüders, M. Börnhorst, O. Deutschmann, Heat transfer during spray/wall interaction with urea water solution: An experimental parameter study, Int. J. Heat Fluid Flow, 78 (2019) 108432.

[7] J. Schmid, I. Zarikos, A. Terzis, N. Roth, B. Weigand, Crystallization of urea from an evaporative aqueous solution sessile droplet at sub-boiling temperatures and surfaces with different wettability, Exp. Therm. Fluid Sci., 91 (2018) 80-88.

[8] W. Brack, B. Heine, F. Birkhold, M. Kruse, O. Deutschmann, Formation of Urea-Based Deposits in an Exhaust System: Numerical Predictions and Experimental Observations on a Hot Gas Test Bench, Emission Contr. Sci. Technol., 2 (2016) 115-123.

[9] M. Börnhorst, S. Langheck, H. Weickenmeier, C. Dem, R. Suntz, O. Deutschmann, Characterization of solid deposits from urea water solution injected into a hot gas test rig, Chem. Eng. J., 377 (2019).

[10] T. Lauer, Preparation of Ammonia from Liquid AdBlue - Modeling Approaches and Future Challenges, Chem. Ing. Tech., 90 (2018) 783-794.

[11] W. Edelbauer, F. Birkhold, T. Rankel, Z. Pavlović, P. Kolar, Simulation of the liquid break-up at an AdBlue injector with the volume-of-fluid method followed by off-line coupled Lagrangian particle tracking, Comput. Fluids, 157 (2017) 294-311.

[12] L.G. Tan, P.F. Feng, S.B. Yang, Y.G. Guo, S.C. Liu, Z.W. Li, CFD studies on effects of SCR mixers on the performance of urea conversion and mixing of the reducing agent, Chem. Eng. Process., 123 (2018) 82-88.

[13] V. Ebrahimian, A. Nicolle, C. Habchi, Detailed modeling of the evaporation and thermal decomposition of urea-water solution in SCR systems, AIChE J., 58 (2012) 1998-2009.

[14] U. Budziankou, M. Börnhorst, C. Kuntz, O. Deutschmann, T. Lauer, Deposit Formation from Urea Injection: a Comprehensive Modeling Approach, Emission Contr. Sci. Technol., 6 (2020) 211-227.

[15] C. Bai, A.D. Gosman, Development of Methodology for Spray Impingement Simulation, SAE International, 1995.

[16] R. Rioboo, C. Tropea, M. Marengo, Outcomes from a drop impact on solid surfaces, Atomization Sprays, 11 (2001) 155-165.

[17] D. Quéré, Leidenfrost Dynamics, Annu. Rev. Fluid Mech., 45 (2013) 197-215.

[18] M. Börnhorst, O. Deutschmann, Single droplet impingement of urea water solution on a heated substrate, Int. J. Heat Fluid Flow, 69 (2018) 55-61.

[19] H. Smith, M. Zöchbauer, T. Lauer, Advanced Spray Impingement Modelling for an Improved Prediction Accuracy of the Ammonia Homogenisation in SCR Systems, SAE International, 2015.

[20] M. Quissek, T. Lauer, O. García-Afonso, S. Fowles, Identification of Film Breakup for a Liquid Urea-Water-Solution and Application to CFD, SAE International, 2019.

[21] I. Malgarinos, N. Nikolopoulos, M. Marengo, C. Antonini, M. Gavaises, VOF simulations of the contact angle dynamics during the drop spreading: Standard models and a new wetting force model, Adv. Colloid Interface Sci., 212 (2014) 1-20.

[22] A.L. Yarin, Drop impact dynamics: Splashing, spreading, receding, bouncing... Annu. Rev. Fluid Mech., 38 (2006) 159-192.

[23] C. Josserand, S.T. Thoroddsen, Drop Impact on a Solid Surface, Annu. Rev. Fluid Mech., 48 (2016) 365-391.

[24] D. Khojasteh, M. Kazerooni, S. Salarian, R. Kamali, Droplet impact on superhydrophobic surfaces: A review of recent developments, Journal of Industrial and Engineering Chemistry, 42 (2016) 1-14.

[25] E. Celia, T. Darmanin, E.T. de Givenchy, S. Amigoni, F. Guittard, Recent advances in designing superhydrophobic surfaces, J. Colloid Interf. Sci., 402 (2013) 1-18.

[26] T. Mao, D.C.S. Kuhn, H. Tran, Spread and rebound of liquid droplets upon impact on flat surfaces, AIChE J., 43 (1997) 2169-2179.

[27] M. Reyssat, A. Pepin, F. Marty, Y. Chen, D. Quere, Bouncing transitions on microtextured materials, Europhys. Lett., 74 (2006) 306-312.

[28] Z. Wang, C. Lopez, A. Hirsa, N. Koratkar, Impact dynamics and rebound of water droplets on superhydrophobic carbon nanotube arrays, Appl. Phys. Lett., 91 (2007).

[29] Y.C. Jung, B. Bhushan, Dynamic Effects Induced Transition of Droplets on Biomimetic Superhydrophobic Surfaces, Langmuir, 25 (2009) 9208-9218.

[30] N.D. Patil, R. Bhardwaj, A. Sharma, Droplet impact dynamics on micropillared hydrophobic surfaces, Exp. Therm. Fluid Sci., 74 (2016) 195-206.

[31] Z.G. Li, Q. Kong, X.Y. Ma, D.Y. Zang, X.H. Guan, X.H. Ren, Dynamic effects and adhesion of water droplet impact on hydrophobic surfaces: bouncing or sticking, Nanoscale, 9 (2017) 8249-8255.

[32] J. Qu, Y.L. Yang, S.S. Yang, D.H. Hu, H.H. Qiu, Droplet impingement on nano-textured superhydrophobic surface: Experimental and numerical study, Appl. Surf. Sci., 491 (2019) 160-170.

[33] C. Antonini, F. Villa, I. Bernagozzi, A. Amirfazli, M. Marengo, Drop Rebound after Impact: The Role of the Receding Contact Angle, Langmuir, 29 (2013) 16045-16050.

[34] Y. Guo, Y. Lian, M. Sussman, Investigation of drop impact on dry and wet surfaces with consideration of surrounding air, Phys. Fluids, 28 (2016) 073303.

[35] D. Caviezel, C. Narayanan, D. Lakehal, Adherence and bouncing of liquid droplets impacting on dry surfaces, Microfluid. Nanofluid., 5 (2008) 469-478.

[36] V.V. Khatavkar, P.D. Anderson, P.C. Duineveld, H.E.H. Meijer, Diffuse-interface modelling of droplet impact, J. Fluid Mech., 581 (2007) 97-127.

[37] Q. Zhang, T. Qian, X.-P. Wang, Phase field simulation of a droplet impacting a solid surface, Phys. Fluids, 28 (2016).

[38] S. Mukherjee, J. Abraham, Investigations of drop impact on dry walls with a lattice-Boltzmann model, J. Colloid Interf. Sci., 312 (2007) 341-354.

[39] J.E. Sprittles, Y.D. Shikhmurzaev, The dynamics of liquid drops and their interaction with solids of varying wettabilities, Phys. Fluids, 24 (2012).

[40] P.G. Bange, R. Bhardwaj, Computational study of bouncing and non-bouncing droplets impacting on superhydrophobic surfaces, Theoretical and Computational Fluid Dynamics, 30 (2016) 211-235.

[41] H. Li, K. Zhang, Dynamic behavior of water droplets impacting on the superhydrophobic surface: Both experimental study and molecular dynamics simulation study, Appl. Surf. Sci., 498 (2019).

[42] Y.J. Liao, P.D. Eggenschwiler, D. Rentsch, F. Curto, K. Boulouchos, Characterization of the urea-water spray impingement in diesel selective catalytic reduction systems, Applied Energy, 205 (2017) 964-975.

[43] Y. Liao, P. Dimopoulos Eggenschwiler, A. Spiteri, L. Nocivelli, G. Montenegro, K. Boulouchos, Fluid Dynamic Comparison of AdBlue Injectors for SCR Applications, SAE International Journal of Engines, 8 (2015) 2303-2311.

[44] S. Jung, I.M. Hutchings, The impact and spreading of a small liquid drop on a non-porous substrate over an extended time scale, Soft Matter, 8 (2012) 2686-2696.

[45] A.M. Briones, J.S. Ervin, S.A. Putnam, L.W. Byrd, L. Gschwender, Micrometer-Sized Water Droplet Impingement Dynamics and Evaporation on a Flat Dry Surface, Langmuir, 26 (2010) 13272-13286.
[46] C.Y. Lim, Y.C. Lam, Phase-field simulation of impingement and spreading of micro-sized droplet on heterogeneous surface, Microfluid. Nanofluid., 17 (2014) 131-148.
[47] X. Cai, H. Marschall, M. Wörner, O. Deutschmann, Numerical Simulation of Wetting Phenomena with a Phase-Field Method Using OpenFOAM®, Chem. Eng. Technol., 38 (2015) 1985-1992.
[48] F. Jamshidi, H. Heimel, M. Hasert, X. Cai, O. Deutschmann, H. Marschall, M. Wörner, On suitability of phase-field and algebraic volume-of-fluid OpenFOAM® solvers for gas–liquid microfluidic applications, Comput. Phys. Commun., 236 (2019) 72-85.
[49] X. Cai, M. Wörner, H. Marschall, O. Deutschmann, Numerical study on the wettability dependent interaction of a rising bubble with a periodic open cellular structure, Catal. Today, 273 (2016) 151-160.
[50] V. Fink, X. Cai, A. Stroh, R. Bernard, J. Kriegseis, B. Frohnapfel, H. Marschall, M. Wörner, Drop bouncing by micro-grooves, Int. J. Heat Fluid Flow, 70 (2018) 271-278.
[51] X. Cai, M. Wörner, H. Marschall, O. Deutschmann, CFD Simulation of Liquid Back Suction and Gas Bubble Formation in a Circular Tube with Sudden or Gradual Expansion, Emission Contr. Sci. Technol., 3 (2017) 289-301.
[52] M. Börnhorst, X. Cai, M. Wörner, O. Deutschmann, Maximum spreading of urea water solution during drop impingement, Chem. Eng. Technol., 42 (2019) 2419-2427.
[53] D. Jacqmin, Contact-line dynamics of a diffuse fluid interface, J. Fluid Mech., 402 (2000) 57-88.
[54] P. Yue, C.F. Zhou, J.J. Feng, Sharp-interface limit of the Cahn-Hilliard model for moving contact lines, J. Fluid Mech., 645 (2010) 279-294.
[55] P. Yue, J.J. Feng, Can diffuse-interface models quantitatively describe moving contact lines?, European Physical Journal Special Topics, 197 (2011) 37-46.
[56] D. Jacqmin, Calculation of Two-Phase Navier-Stokes Flows Using Phase-Field Modeling, J. Comput. Phys., 155 (1999) 96-127.
[57] F. Bai, X. He, X. Yang, R. Zhou, C. Wang, Three dimensional phase-field investigation of droplet formation in microfluidic flow focusing devices with experimental validation, Int. J. Multiph. Flow, 93 (2017) 130-141.
[58] P. Seppecher, Moving contact lines in the Cahn-Hilliard theory, International Journal of Engineering Science, 34 (1996) 977-992.
[59] W. Villanueva, G. Amberg, Some generic capillary-driven flows, Int. J. Multiph. Flow, 32 (2006) 1072-1086.
[60] H. Kusumaatmaja, E.J. Hemingway, S.M. Fielding, Moving contact line dynamics: from diffuse to sharp interfaces, J. Fluid Mech., 788 (2016) 209-227.
[61] R.G. Cox, The Dynamics of the Spreading of Liquids on a Solid-Surface. Part 1. Viscous-Flow, J. Fluid Mech., 168 (1986) 169-194.
[62] J.H. Kim, H.P. Kavehpour, J.P. Rothstein, Dynamic contact angle measurements on superhydrophobic surfaces, Phys. Fluids, 27 (2015).
[63] M. Wörner, X. Cai, H. Alla, P. Yue, A semi-analytical method to estimate the effective slip length of spreading spherical-cap shaped droplets using Cox theory, Fluid Dyn. Res., 50 (2018).
[64] A. Carlson, M. Do-Quang, G. Amberg, Modeling of dynamic wetting far from equilibrium, Phys. Fluids, 21 (2009) 121701-121701- 121701-121704.
[65] P. Yue, J.J. Feng, Wall energy relaxation in the Cahn-Hilliard model for moving contact lines, Phys. Fluids, 23 (2011) 012106.
[66] Y. Wu, F. Wang, M. Selzer, B. Nestler, Investigation of Equilibrium Droplet Shapes on Chemically Striped Patterned Surfaces Using Phase-Field Method, Langmuir, 35 (2019) 8500-8516.
[67] H. Marschall, L. Cornolti, X. Cai, M. Wörner, phaseFieldFoam - Conservative finite volume discretization of the two-phase Navier-Stokes Allen-Cahn and Cahn-Hilliard equations on general grids with applications to dynamic wetting, (2021) In preparation.

[68] H. Jasak, H.G. Weller, A.D. Gosman, High resolution NVD differencing scheme for arbitrarily unstructured meshes, Int. J. Numer. Methods Fluids, 31 (1999) 431-449.

[69] Y.Z. Shen, J. Tao, G.Y. Wang, C.L. Zhu, H.F. Chen, M.M. Jin, Y.H. Xie, Bioinspired Fabrication of Hierarchical-Structured Superhydrophobic Surfaces To Understand Droplet Bouncing Dynamics for Enhancing Water Repellency, J. Phys. Chem. C, 122 (2018) 7312-7320.

[70] S.J. Lin, B.Y. Zhao, S. Zou, J.W. Guo, Z. Wei, L. Chen, Impact of viscous droplets on different wettable surfaces: Impact phenomena, the maximum spreading factor, spreading time and post-impact oscillation, J. Colloid Interf. Sci., 516 (2018) 86-97.

[71] D. Richard, C. Clanet, D. Quéré, Contact time of a bouncing drop, Nature, 417 (2002) 811.

[72] Y. Renardy, S. Popinet, L. Duchemin, M. Renardy, S. Zaleski, C. Josserand, M.A. Drumright-Clarke, D. Richard, C. Clanet, D. Quere, Pyramidal and toroidal water drops after impact on a solid surface, J. Fluid Mech., 484 (2003) 69-83.

[73] P. Chantelot, A.M. Moqaddam, A. Gauthier, S.S. Chikatamarla, C. Clanet, I.V. Karlin, D. Quéré, Water ring-bouncing on repellent singularities, Soft Matter, 14 (2018) 2227-2233.

[74] L. Chen, L. Li, Z.-D. Li, K. Zhang, Submillimeter-Sized Bubble Entrapment and a High-Speed Jet Emission during Droplet Impact on Solid Surfaces, Langmuir, 33 (2017) 7225-7230.

[75] H. Ding, E.Q. Li, F.H. Zhang, Y. Sui, P.D.M. Spelt, S.T. Thoroddsen, Propagation of capillary waves and ejection of small droplets in rapid droplet spreading, J. Fluid Mech., 697 (2012) 92-114.

[76] I.S. Bayer, C.M. Megaridis, Contact angle dynamics in droplets impacting on flat surfaces with different wetting characteristics, J. Fluid Mech., 558 (2006) 415-449.

[77] T.A. Elliott, D.M. Ford, Dynamic Contact Angles .7. Impact Spreading of Water Drops in Air and Aqueous-Solutions of Surface-Active Agents in Vapor on Smooth Paraffin Wax Surfaces, Journal of the Chemical Society-Faraday Transactions I, 68 (1972) 1814-&.

[78] P.G. Pittoni, Y.-C. Lin, R.-J. Wang, T.-S. Yu, S.-Y. Lin, Bubbles entrapment for drops impinging on roughness effect polymer surfaces: The, Exp. Therm. Fluid Sci., 62 (2015) 183-191.

[79] T.-V. Nguyen, M. Ichiki, Bubble entrapment during the recoil of an impacting droplet, Microsystems & Nanoengineering, 6 (2020) 36.

[80] S.T. Thoroddsen, T.G. Etoh, K. Takehara, Air entrapment under an impacting drop, J. Fluid Mech., 478 (2003) 125-134.

[81] S.T. Thoroddsen, T.G. Etoh, K. Takehara, N. Ootsuka, A. Hatsuki, The air bubble entrapped under a drop impacting on a solid surface, J. Fluid Mech., 545 (2005) 203-212.

[82] J.S. Lee, B.M. Weon, J.H. Je, K. Fezzaa, How Does an Air Film Evolve into a Bubble During Drop Impact?, Phys. Rev. Lett., 109 (2012).

[83] R.C.A. van der Veen, T. Tran, D. Lohse, C. Sun, Direct measurements of air layer profiles under impacting droplets using high-speed color interferometry, Physical Review E, 85 (2012).

[84] C.W. Visser, P.E. Frommhold, S. Wildeman, R. Mettin, D. Lohse, C. Sun, Dynamics of high-speed micro-drop impact: numerical simulations and experiments at frame-to-frame times below 100 ns, Soft Matter, 11 (2015) 1708-1722.

[85] Z. Jian, C. Josserand, S. Popinet, P. Ray, S. Zaleski, Two mechanisms of droplet splashing on a solidsubstrate, J. Fluid Mech., 835 (2018) 1065-1086.

[86] J.C. Bird, R. Dhiman, H.-M. Kwon, K.K. Varanasi, Reducing the contact time of a bouncing drop, Nature, 503 (2013) 385-388.

[87] S. Halonen, T. Kangas, M. Haataja, U. Lassi, Urea-Water-Solution Properties: Density, Viscosity, and Surface Tension in an Under-Saturated Solution, Emission Contr. Sci. Technol., 3 (2017) 161-170.

[88] J. Dörnhöfer, M. Börnhorst, C. Ates, N. Samkhaniani, J. Pfeil, M. Wörner, R. Koch, H.-J. Bauer, O. Deutschmann, B. Frohnapfel, T. Koch, A Holistic View on Urea Injection for NOx Emission Control: Impingement, Re-atomization, and Deposit Formation, Emission Contr. Sci. Technol., 6 (2020) 228-243.

[89] R. Rioboo, M. Marengo, C. Tropea, Time evolution of liquid drop impact onto solid, dry surfaces, Exp. Fluids, 33 (2002) 112-124.

[90] J. Oh, K. Lee, Spray characteristics of a urea solution injector and optimal mixer location to improve droplet uniformity and NOx conversion efficiency for selective catalytic reduction, Fuel, 119 (2014) 90-97.

[91] A. Varna, A.C. Spiteri, Y.M. Wright, P.D. Eggenschwiler, K. Boulouchos, Experimental and numerical assessment of impingement and mixing of urea-water sprays for nitric oxide reduction in diesel exhaust, Applied Energy, 157 (2015) 824-837.

[92] H.Y. Kim, J.H. Chun, The recoiling of liquid droplets upon collision with solid surfaces, Phys. Fluids, 13 (2001) 643-659.

[93] T.C. de Goede, K.G. de Bruin, N. Shahidzadeh, D. Bonn, Predicting the maximum spreading of a liquid drop impacting on a solid surface: Effect of surface tension and entrapped air layer, Phys. Rev. Fluids, 4 (2019).

[94] R.E. Ford, C.G.L. Furmidge, Impact and spreading of spray drops on foliar surfaces, Wetting, Society of Chemical Industry, London, 1967.

[95] S.E. Bechtel, D.B. Bogy, F.E. Talke, Impact of a Liquid-Drop against a Flat Surface, IBM J. Res. Dev., 25 (1981) 963-971.

[96] E.W. Collings, A.J. Markworth, J.K. McCoy, J.H. Saunders, Splat-quench solidification of freely falling liquid-metal drops by impact on a planar substrate, Journal of Materials Science, 25 (1990) 3677-3682.

[97] S. Chandra, C.T. Avedisian, On the collision of a droplet with a solid surface, Proceedings of the Royal Society of London. Series A: Mathematical and Physical Sciences, 432 (1991) 13-41.

[98] J. Fukai, Y. Shiiba, T. Yamamoto, O. Miyatake, D. Poulikakos, C.M. Megaridis, Z. Zhao, Wetting Effects on the Spreading of a Liquid Droplet Colliding with a Flat Surface - Experiment and Modeling, Phys. Fluids, 7 (1995) 236-247.

[99] M. Pasandideh-Fard, Y.M. Qiao, S. Chandra, J. Mostaghimi, Capillary effects during droplet impact on a solid surface, Phys. Fluids, 8 (1996) 650-659.

[100] P. Attane, F. Girard, V. Morin, An energy balance approach of the dynamics of drop impact on a solid surface, Phys. Fluids, 19 (2007).

[101] Y. Yonemoto, T. Kunugi, Analytical consideration of liquid droplet impingement on solid surfaces, Scientific Reports, 7 (2017).

[102] J.B. Lee, D. Derome, A. Dolatabadi, J. Carmeliet, Energy Budget of Liquid Drop Impact at Maximum Spreading: Numerical Simulations and Experiments, Langmuir, 32 (2016) 1279-1288.

[103] B.L. Scheller, D.W. Bousfield, Newtonian drop impact with a solid surface, AIChE J., 41 (1995) 1357-1367.

[104] I.V. Roisman, R. Rioboo, C. Tropea, Normal impact of a liquid drop on a dry surface: model for spreading and receding, Proceedings of the Royal Society a-Mathematical Physical and Engineering Sciences, 458 (2002) 1411-1430.

[105] J. Madejski, Solidification of Droplets on a Cold Surface, Int. J. Heat Mass Transf., 19 (1976) 1009-1013.

[106] C. Clanet, C. Béguin, D. Richard, D. Quéré, Maximal deformation of an impacting drop, J. Fluid Mech., 517 (2004) 199-208.

[107] J. Seo, J.S. Lee, H.Y. Kim, S.S. Yoon, Empirical model for the maximum spreading diameter of low-viscosity droplets on a dry wall, Exp. Therm. Fluid Sci., 61 (2015) 121-129.

[108] C. Antonini, A. Amirfazli, M. Marengo, Drop impact and wettability: From hydrophilic to superhydrophobic surfaces, Phys. Fluids, 24 (2012) 102104.

[109] Y. Wu, Numerical Simulation of Droplet Impact and Rebound on a Wall, Master thesis, Karlsruhe Institute of Technology (KIT), 2017, doi: 10.5445/ir/1000079141.

[110] R. Rioboo, M. Voue, A. Vaillant, J. De Coninck, Drop Impact on Porous Superhydrophobic Polymer Surfaces, Langmuir, 24 (2008) 14074-14077.

[111] S. Yun, Bouncing of an ellipsoidal drop on a superhydrophobic surface, Scientific Reports, 7 (2017) 17699.

[112] B.M. Law, S.P. McBride, J.Y. Wang, H.S. Wi, G. Paneru, S. Betelu, B. Ushijima, Y. Takata, B. Flanders, F. Bresme, H. Matsubara, T. Takiue, M. Aratono, Line tension and its influence on droplets and particles at surfaces, Prog. Surf. Sci., 92 (2017) 1-39.
[113] R.D. Schroll, C. Josserand, S. Zaleski, W.W. Zhang, Impact of a Viscous Liquid Drop, Phys. Rev. Lett., 104 (2010).

Supplemental Material A

Comparison of computed drop shapes for Case A. Left column: $Cn = 0.01$, right column: $Cn = 0.02$.
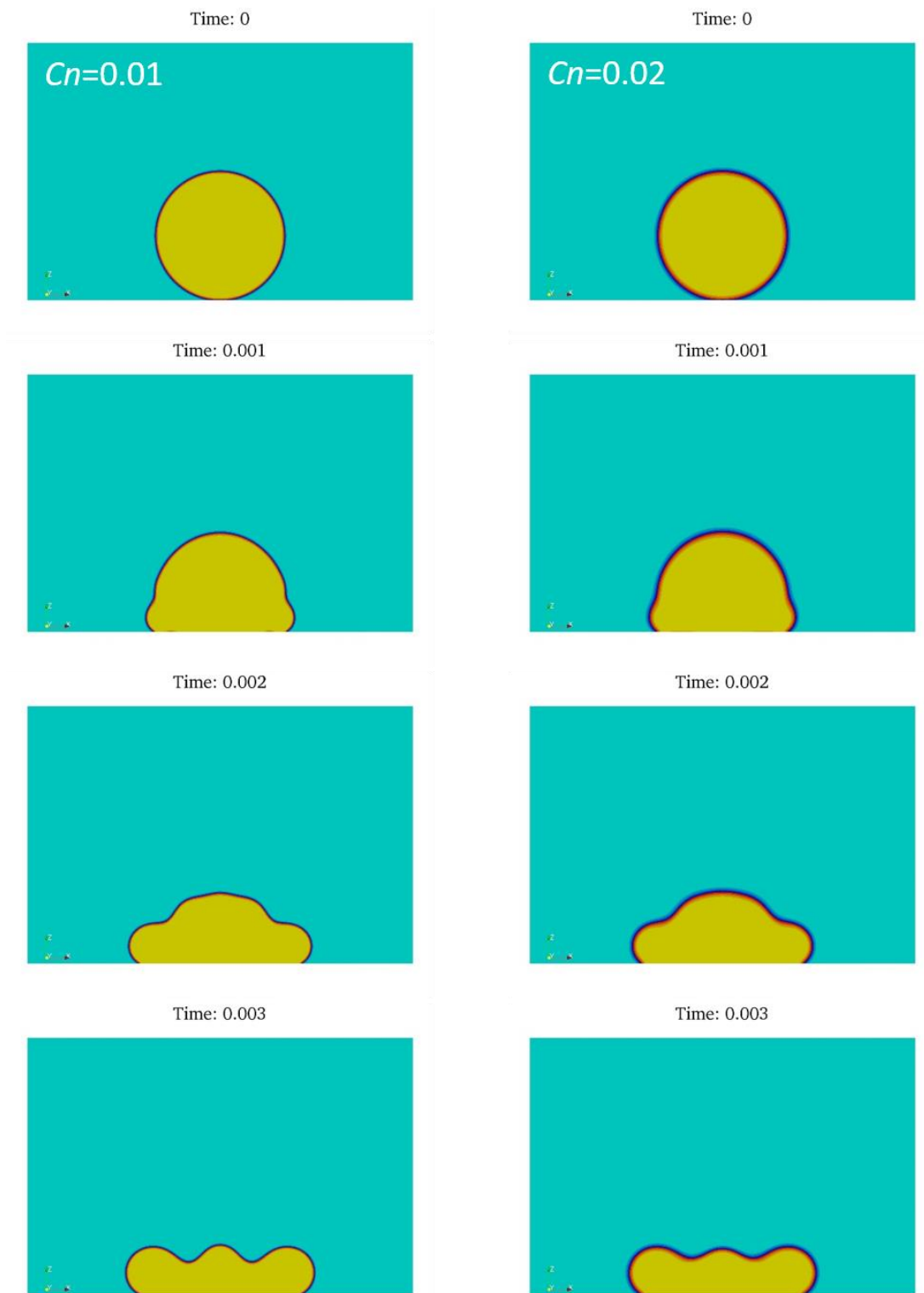
Time: 0.004   Time: 0.004
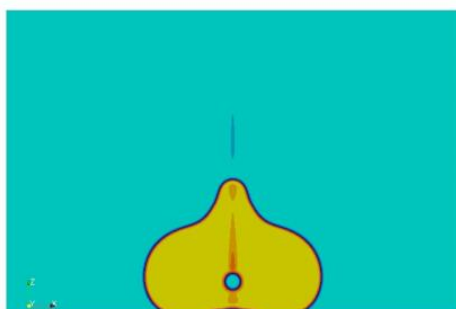
Time: 0.005   Time: 0.005
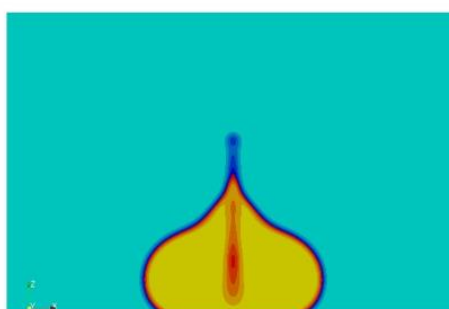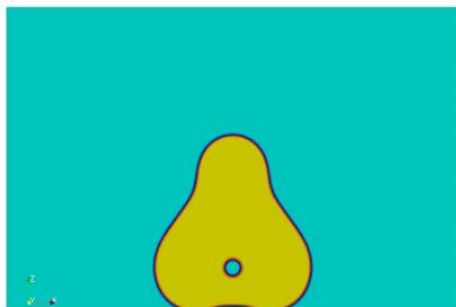
Time: 0.006   Time: 0.006

Time: 0.007   Time: 0.007
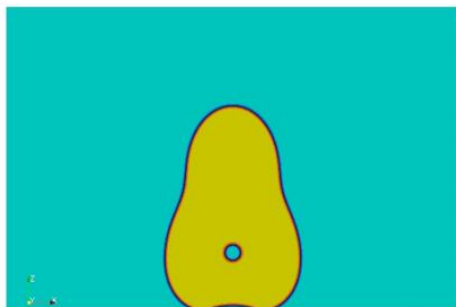
Cn=0.01
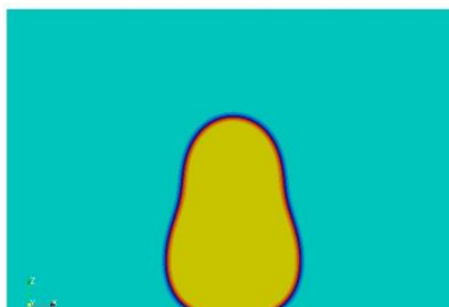
Cn=0.02

Time: 0.008
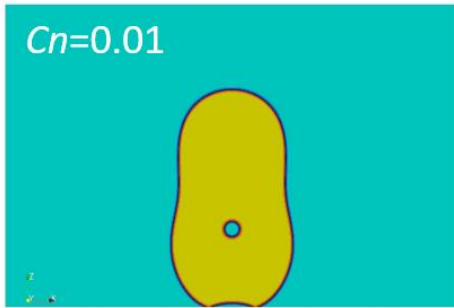
Cn=0.01
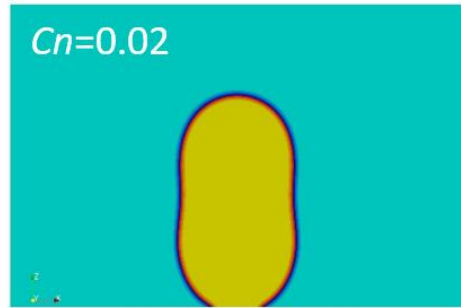
Time: 0.008
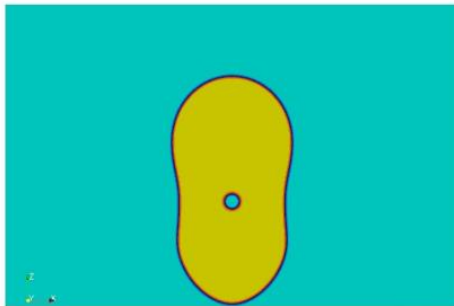
Cn=0.02

Time: 0.009

Time: 0.009
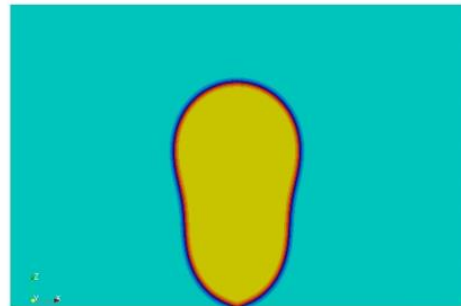
Time: 0.01
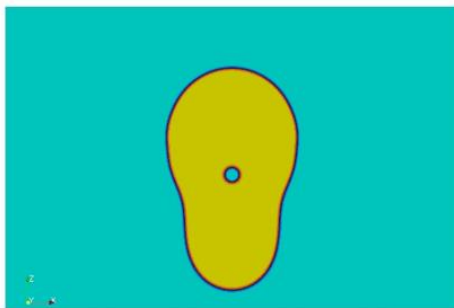
Time: 0.01
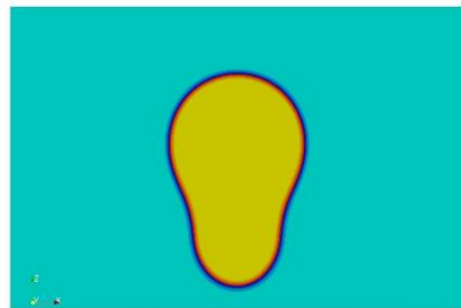
Time: 0.011

Time: 0.011
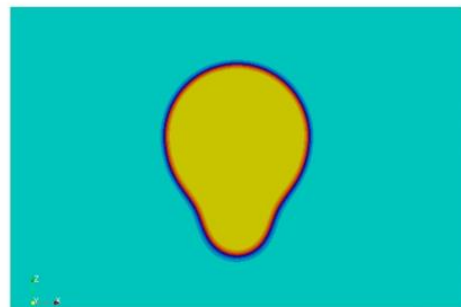
Bubble formation in simulation with $Cn = 0.01$. Left column: $Cn = 0.01$, right column: $Cn = 0.02$.
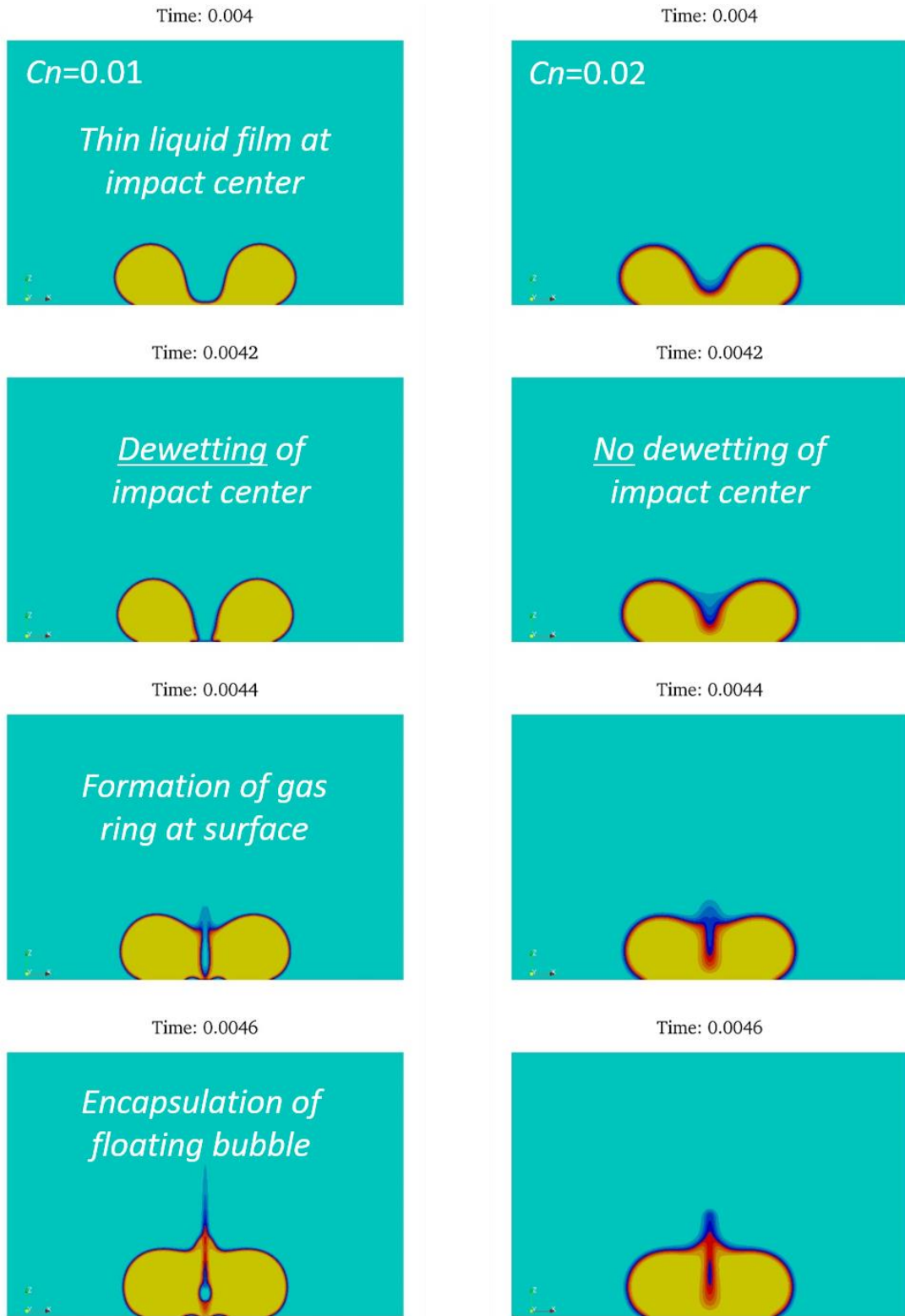
Drop bouncing in simulation with $Cn = 0.01$. Left column: $Cn = 0.01$, right column: $Cn = 0.02$.
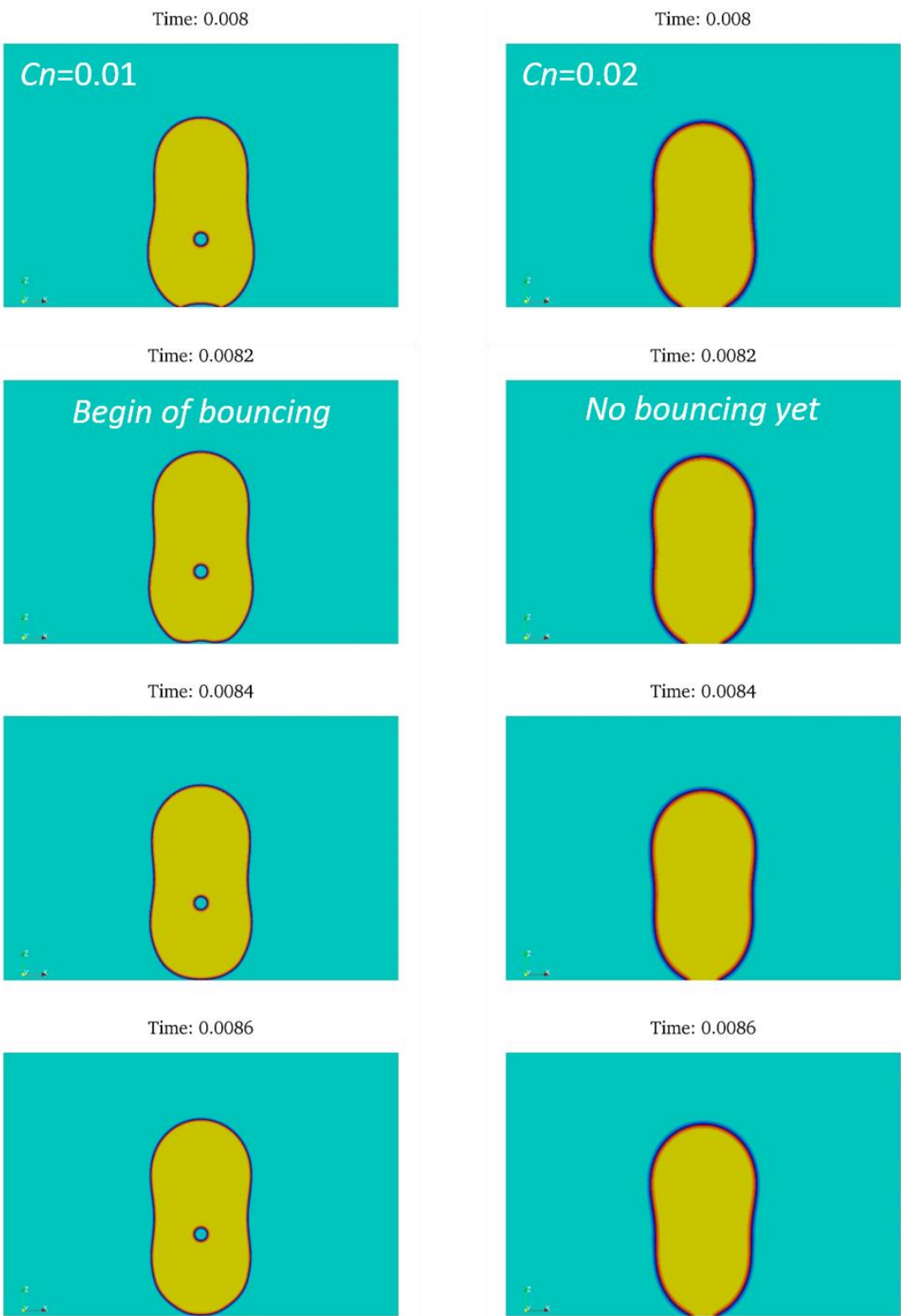
Drop bouncing in simulation with $Cn = 0.02$. Left column: $Cn = 0.01$, right column: $Cn = 0.02$.
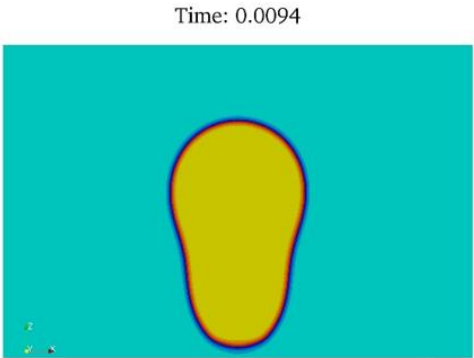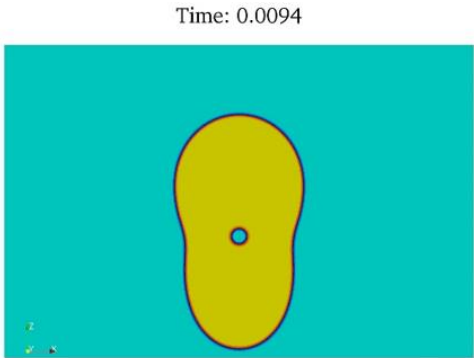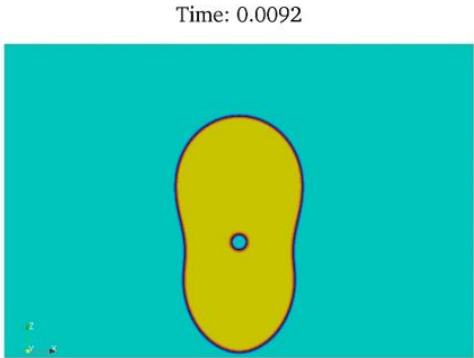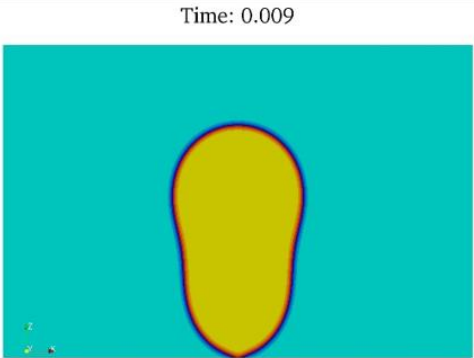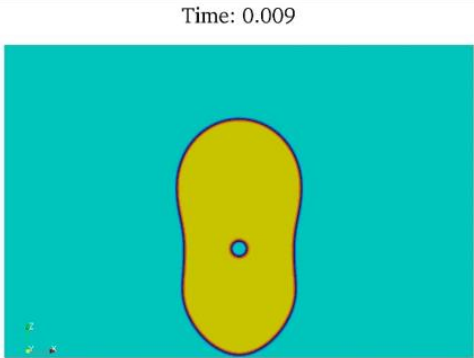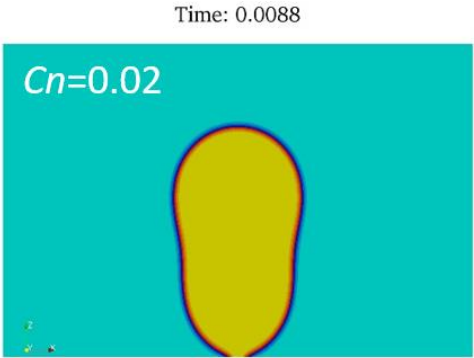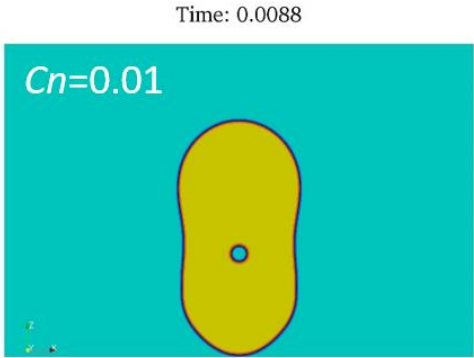
Supplemental Material B: Model of Caviezel et al. [1]

Neglecting gravity, the total equilibrium energy of a free spherical drop with radius R_{sphere} consists only of surface energy and is given by

$$E_{\text{sphere}} = \sigma A_{\text{sphere}}^{\text{LG}} = 4\pi\sigma R_{\text{sphere}}^2 \tag{1}$$

The equilibrium surface energy of a drop adhering to the wall in the form of a spherical cap is

$$E_{\text{cap}} = \sigma A_{\text{cap}}^{\text{LG}} + A_{\text{cap}}^{\text{SL}}(\gamma_{\text{SL}} - \gamma_{\text{SG}}) \tag{2}$$

Introducing Young's equation

$$\gamma_{\text{SL}} - \gamma_{\text{SG}} = -\sigma\cos\theta \tag{3}$$

into Eq. (2) gives

$$E_{\text{cap}} = \sigma A_{\text{cap}}^{\text{LG}} - \sigma A_{\text{cap}}^{\text{SL}}\cos\theta \tag{4}$$

It is

$$A_{\text{cap}}^{\text{LG}} = 2\pi r_{\text{cap}} h_{\text{cap}} \tag{5}$$

where r_{cap} is the spherical cap radius and h_{cap} the height of the spherical cap[1]. Furthermore, it is

$$A_{\text{cap}}^{\text{SL}} = \pi a_{\text{cap}}^2 \tag{6}$$

where a_{cap} is the radius of the circular solid-liquid interface. Introducing Eq. (5) and Eq. (6) into Eq. (4) gives

$$E_{\text{cap}} = 2\pi\sigma r_{\text{cap}} h_{\text{cap}} - \pi\sigma a_{\text{cap}}^2\cos\theta = \pi\sigma\left(2r_{\text{cap}} h_{\text{cap}} - a_{\text{cap}}^2\cos\theta\right) \tag{7}$$

The height and wetted radius of the spherical cap can also be written as

$$h_{\text{cap}} = (1 - \cos\theta)r_{\text{cap}} \tag{8}$$
$$a_{\text{cap}} = r_{\text{cap}}\sin\theta \tag{9}$$

Introducing the latter two equations into Eq. (7) gives

$$E_{\text{cap}} = \pi\sigma r_{\text{cap}}^2(2 - 2\cos\theta - \cos\theta\sin^2\theta) = \pi\sigma r_{\text{cap}}^2(2 - 3\cos\theta + \cos^3\theta) \tag{10}$$

The difference in surface energy is then given by

$$\Delta E = E_{\text{sphere}} - E_{\text{cap}} = 4\pi\sigma R_{\text{sphere}}^2 - \pi\sigma r_{\text{cap}}^2(2 - 3\cos\theta + \cos^3\theta) \tag{11}$$

Assuming the volume of the spherical cap given by

---

[1] Note that is nomenclature is in contrast to Caviezel et al. where h_{C} denotes the height of the missing segment of the spherical cap. Both quantities are related as $h_{\text{C}} = 2r - h$.

$$V_{cap} = \frac{\pi}{3}(2 - 3\cos\theta + \cos^3\theta)r_{cap}^3 \tag{12}$$

being equal to the sphere volume $V_{sphere} = 4\pi R_0^3 / 3$ yields

$$\frac{\pi}{3}(2 - 3\cos\theta + \cos^3\theta)r_{cap}^3 = \frac{4\pi}{3}R_{sphere}^3 \tag{13}$$

and

$$r_{cap}^3 = 4R_{sphere}^3(2 - 3\cos\theta + \cos^3\theta)^{-1} \tag{14}$$

so that

$$r_{cap} = 2R_{sphere}\left[2(2 - 3\cos\theta + \cos^3\theta)\right]^{-1/3} = 2R_{sphere}\left[2(1 - \cos\theta)(2 - \cos\theta - \cos^2\theta)\right]^{-1/3} \tag{15}$$

which corresponds to Eq. (8) of Caviezel et al. [1]. Introducing Eq. (15) into Eq. (11) yields

$$\begin{aligned}\Delta E &= 4\pi\sigma R_{sphere}^2 - 4\pi\sigma R_{sphere}^2(2 - 3\cos\theta + \cos^3\theta)\left[2(1 - \cos\theta)(2 - \cos\theta - \cos^2\theta)\right]^{-2/3} \\ &= 4\pi\sigma R_{sphere}^2\left\{1 - (2 - 3\cos\theta + \cos^3\theta)\left[2(1 - \cos\theta)(2 - \cos\theta - \cos^2\theta)\right]^{-2/3}\right\}\end{aligned} \tag{16}$$

This corresponds to Eq. (B.5) in the master thesis of Wu [2].

References

1. Caviezel, D., C. Narayanan, and D. Lakehal, *Adherence and bouncing of liquid droplets impacting on dry surfaces.* Microfluidics and Nanofluidics, 2008. **5**(4): p. 469-478.

2. Wu, Y., *Numerical Simulation of Droplet Impact and Rebound on a Wall.* 2017: Karlsruhe Institute of Technology (KIT), doi: 10.5445/ir/1000079141.